People's Democratic Republic of Algeria
الجمهورية الجزائرية الديمقراطية الشعبية
Ministry of higher education and scientific research
وزارة التعليم العالي والبحث العلمي
University saad dahleb of blida 1
جامعة سعد دحلب البليدة 1

Faculty of sciences
كلية العلوم
Physics department
قسم الفيزياء

Option: Nanophysics

Theme:

Elaboration and characterization of nanocrystals based iron sulfide Fe_xS_y for energy conversion

By: Sekrane Noraya

Jury member:

Dr. Salah Eddine AOUDJ	MCA	USDB-1	President
Dr. Abderrahmane YOUNES	MRA	CRTI	Examiner
Dr. Nouredine OUARAB	MRA, HDR	CRTSE	Supervisor
Dr. Abd-el-Kader HASSEIN-BEY	MCB	USDB-1	Co-supervisor

2022

Abstact

Iron disulfide FeS_2 known as pyrite have attracted attention in many fields for its interesting properties, expanding their fields of application in energy conversion technology. Therefore, we are interested in synthesizing FeS_2 nanostructures by an accessible elaboration method based on thermal evaporation. Iron/nickel thin films were prepared on ceramic $Al_2Si_2O_5$-$(OH)_4$. This was followed by a sulfidation annealing. X-ray diffraction (XRD) characterization revealed the presence of a Fe-S bonds relative of structural pyrite phase, which was confirmed by SEM analysis of chemical components and showed the elongated cubic morphology wanted; other characterization techniques are used to get an overview of the properties required for this work. In particular, photoluminescence spectra are used to determine band gaps, UV-Vis-IR to determine absorbance and gas treatment to determine the sensitivity to toxic gases.

Résumé

Le disulfure de fer FeS_2, connu sous le nom de pyrite, a attiré l'attention dans de nombreux domaines pour ses propriétés intéressantes, élargissant leurs champs d'application dans la technologie de conversion de l'énergie. Par conséquent, nous nous sommes intéressés à la synthèse de nanostructures de FeS2 par une méthode d'élaboration accessible basée sur l'évaporation thermique. Des films minces de fer/nickel ont été préparés sur la céramique $Al_2Si_2O_5$-$(OH)_4$, suivis d'un recuit de sulfuration. La caractérisation par diffraction des rayons X (DRX) a révélé la présence d'une liaison Fe-S relative à la phase pyrite structurale, ce qui a été confirmé par l'analyse EDS/SEM des composants chimiques et a montré la morphologie cubique allongée recherchée ; d'autres techniques de caractérisation sont utilisées pour avoir un aperçu des propriétés requises pour ce travail. En particulier, les spectres de photoluminescence sont utilisés pour déterminer les bandes interdites, les UV-Vis-IR pour déterminer l'absorbance et le traitement au gaz pour déterminer la sensibilité aux gaz toxiques.

ملخص

جذب ثنائي كبريتيد الحديد FeS_2 المعروف باسم البيريت الانتباه في العديد من المجالات لخصائصه المثيرة للاهتمام مما أدى إلى توسيع مجالات تطبيقها في تكنولوجيا تحويل الطاقة. لذلك، أصبحنا مهتمين بتصنيع الرقائق النانوية بطريقة التبخر الحراري .تم إعداد أغشية رقيقة من الحديد على السيراميك تبع ذلك التلدين بالكبريت. كشف توصيف حيود الأشعة السينية عن وجود مرحلة بيريت هيكلية، والتي أكدتها مسح المجهر الإلكتروني وأظهرت التشكل الدقيق المطلوب00؛ وتستخدم تقنيات توصيف أخرى للحصول على لمحة عامة عن الخصائص المطلوبة لهذا العمل. على وجه الخصوص، يتم استخدام أطياف الإضاءة الضوئية لتحديد فجوات النطاق، والأشعة فوق البنفسجية فوق البنفسجية لتحديد الامتصاص ومعالجة الغاز لتحديد الحساسية للغازات السامة .

Dedications

I dedicate this work:

To my dear parents whom i love very much, may god give them good health and long life,

To my sister,

My brothers,

My fiance,

and my friends, who have always been there for me from near and far,

To all the people who contributed to the realization of this project

To myself,

I thank you for everything

Acknowledgments

First of all, I thank the God, almighty, to have given me the strength to arrive here.

I would like to express all my gratitude to my thesis director, Mr. ***Nouredine OUARAB****. I thank him for having framed, guided, helped and advised me.*

I address my sincere thanks to all the professors, contributors and all the people who by their words, their writings, their advice and their criticisms guided my reflections and agreed to meet me and to answer my questions during my research.

I thank my dearest parents, who have always been there for me. I thank my family and friends, for their unconditional support and encouragement which has been of great help.

To all of them, I present my thanks, my respect and my gratitude.

Nomenclature

XRD	X-ray diffraction
SEM	Scanning electron microscopy
EDS	Energy dispersive spectroscopy
XRF	X-ray fluorescence
FTIR	Fourier transformation infrared
AFM	Atomic force microscopy
GC	Gas chromatography
TMDC	Transition metal dichalcogenide
VBM	Valence band maximum
CBM	Conduction band minimum
LMTO-ASA method	linear muffin-tin orbital method
eV	Electron volts
nvdW	non vander waals
FE	Faraday efficiency
PL	Photoluminescence
TL	Thermoluminescence
UV	Ultraviolet
Vis	Visible
NiR	Near infrared
Gy	Gray
ZT	Figure of merit
PF	Power factor
SBC	Solution based chemistry
CBD	Chemical bath deposition
PVD	Physical vapor deposition
NCs	Nanocrystals

Contents

List of figures

Chapter 1:

Chapter 2:

Chapter 3:

List of tables

Chapter 1:

Chapter 3:

1. General introduction :

Most people have heard of the term "fool's gold," which refers to pyrite, a coppery yellow mineral. The name of pyrite is derived from the Greek word Pyr, which means fire, and refers to the spark-forming properties when touched by a flint. The brilliant crystals of this mineral have attracted attention in many different cultures, and it's almost gold-like appearance has led to confusion [1]. It was discovered by Dr. Johnathan Jacobo in 1432. Pyrite, which is FeS_2, is one of the chalcogenide semiconductors having one of the very first cubic crystal structures to be determined by the X-ray diffraction method until the beginning of the 20^{th} century.

In the past, pyrite occupies a unique place in human history. It has long been a source of metal and sulfur, and both commodities have been the key to our civilization. Considered as a promising material that fulfills the requirement of modern material science and which has attracted increasingly attention as a material for multiple uses such as energy storage, energy conversion, battery cathodes, photovoltaic and photo-electrochemical applications due to its favorable electronic and optical properties. Iron disulfide (FeS_2) has two common crystal structures: cubic system pyrite and orthorhombic system marcasite. So, FeS_2 became the interest center has become the focus of several industrial and academic communities as a competitive candidate for working material. Scientific interest in these materials has increased and in this sense, transition metal disulfides are particularly interesting for solving today's problems, as they allow combining techniques for exhaust gas treatment.

Yet, 3^d transition metals are a perfect and inexpensive alternative to noble metals in electro-catalyst technologies, with the general formula MX_2, where typically M = Fe, Co or Ni and X = S or Se); they are commonly proposed in CO_2 reduction to help solve many environmental dilemmas, e.g.: melting icebergs, sea level rise, acid rain…[2]

Even further, FeS_2 can be implicated in chemical reactions to speed up their process faster than otherwise. One crucial requirement for these reactions is the electronic inter-conversion of organic molecules, which is required to fill or complete a metabolism. For example, iron sulfide minerals can catalyze (accelerate) the reaction of these compounds to

produce organic acids from CO_2, it acts as a highly efficient catalyst in emerging clean and renewable energy technologies. [3]

However, current technology is leaning towards the development of nanoscale materials governed by the term of quantum confinement, for which they exhibit specific physical properties that exist neither in bulk nor on the surface. FeS_2 nanocrystals, nanowires and nanotubes have been synthesized by several methods, including chemicals such as bath deposition, electrolysis, sol-gel, etc. Most of these techniques have been motivated by efficient synthesis routes to control the morphology, stability and dispersion of particles and clusters. Many common methods including hydrothermal, hot injection, solvo-thermal, and sulfurization have also been used for the preparation of high quality FeS_2 nano-structures.

In this memory, we will be elaborating thin films based on sulfide and then analyzing them by structural, morphological, optical, thermo luminescence and electrochemical characterizations using different techniques such as X-ray diffraction (XRD), SEM analysis by EDS, XRF and FTIR.

Finally, analyses by AFM (Atomic Force Microscopy) can be considered for the study of the surface morphology and comparing the results. All this work will be done in order to study the phenomena of gas conversion, by the use of the gas phase chromatography GPC.

This memory is composed of the following three chapters, the first defines the FeS_2 and describes its structure and mentions its different properties; the second illustrate different thin layer deposition techniques used to synthesis the substrate and the different characterizations procedures; and finally the third chapter, only speaks about the results obtained, their interpretation and the future prospective.

Chapter 1:

1.1. Definition :

Iron disulfide has attracted particular interest in recent years because of the material's abundance, non-toxicity, and low cost material, band gap of 0.95 eV, and high optical absorption coefficient α, which describes the amount of light absorbed by a material in order of thickness [4].

Transition metal disulfides of the M_xS_y type (M= Fe, Co, Ni, Cu, Zn), have a structure, in which the metal atoms are linked octahedrally to the adjacent sulfur atoms [6]. They crystallize in the pyrite structure of space group $Pa\overline{3}$, where the metal atoms occupy the sites at the vertices of the cube. The axes of the four S_2 pairs of the unit cell are oriented along the four diagonal directions where each cation is surrounded by six anions and the nearest neighbor atoms form an octahedron. Pyrite-type M_xS_y are diverse, depending on the number of 3^d electrons of the transition metals. This diversity results from the different properties of the MxSy [8], such as, FeS_2, CoS_2 is a ferromagnetic, NiS_2 is an antiferromagnetic semiconductor, CuS_2 is metallic changing state to superconductivity at low temperature and ZnS_2 is a non-magnetic insulator with a large band gap.

Other transition metal dichalcogenide (TMDC) materials can also be considered as metal disulfides and exhibit layered structures in the form of X-M-X with chalcogen atoms (X) and transition metal atoms (M); several structural phases exist, resulting from different coordination spheres of transition metal atoms. The two common structural phases are characterized by either trigonal prismatic (2H) or octahedral (1T) coordination of metal atoms. These structural phases can also be viewed in terms of different stacking orders of the three atomic planes (chalcogen–metal–chalcogen) forming the individual layers of these materials. [5-6]

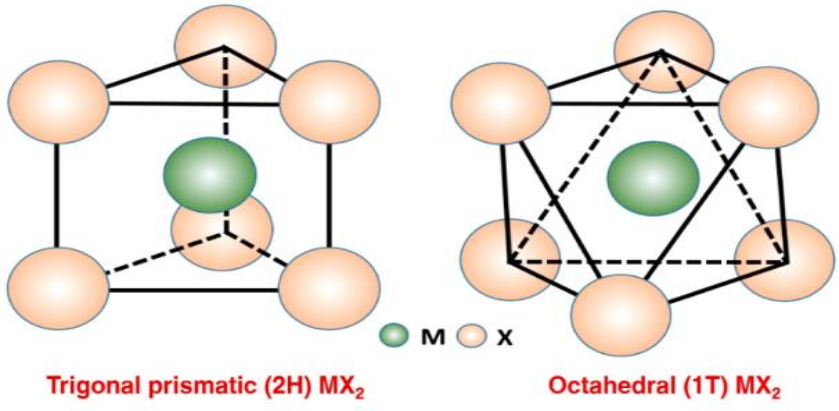

Fig.1.1. Unit cell structures of 2H-MX_2 and 1T-MX_2. [6]

1.1.1 Crystallography of 3^d metal disulfide

FeS_2 has two common crystal structures, Pyrite cubic system with a lattice parameter a=b=c= 5.412Å, group space 205 $Pa\overline{3}$ and a band gap = 0.95 eV. And marcasite orthorhombic system with a= 4.443 Å, b = 5.425 Å, c = 3.387 Å, space group 58 Pnnm and a band gap = 0.34 eV. The S-S bond lengths in the two polymorphs are 2.16 and 2.21 Å, respectively. [5]

In terms of lattice parameters, the crystal structure is similar to rock salt with face center cubic FCC [7] and in both structures, the Fe atoms are coordinated with six nearest-neighbored sulfur dumbbells (S_2^{-2}) the difference remains in positions of Fe atoms; case of pyrite, atoms are located at the corners and in the center of the faces of the cubic, but for marcasite, Fe is located in the corners and in the middle of the center of the orthorhombic.

In pyrite, the S-Fe-S triplets are disposed respectively to the diagonal of the cubic unit-cell space and are oriented alternately. In marcasite, it is the same except that the S-Fe-S triplets are all oriented in the same direction. [8]

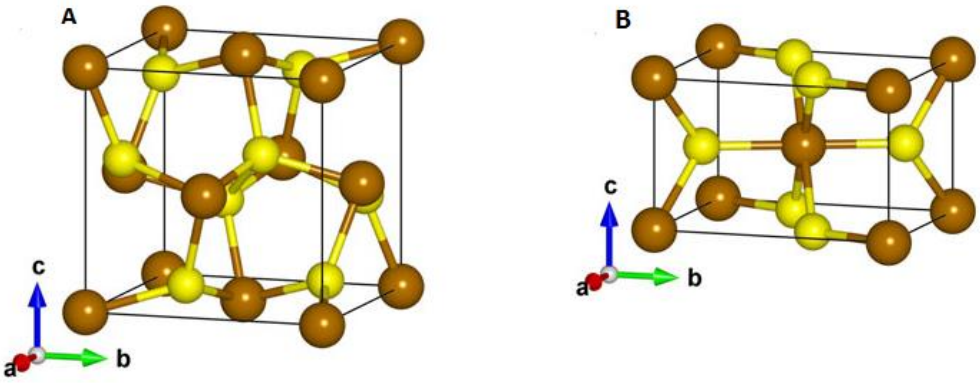

Fig.1.2. Lattice structures (A, B) of pyrite (on the left) and marcasite (on the right) phases of FeS_2. Brown and yellow spheres represent Fe and S atoms, respectively. [5]

Iron pyrite FeS_2, is the most studied structure, it represents the compound with a simple cubic crystallographic structure among the first crystal structures determined by X-ray diffraction. It belongs to the crystallographic space group $Pa\overline{3}$ and is designated by the notation Strukturbericht C2. Under standard thermodynamic conditions, the lattice constant a_{FeS2} of the stoichiometric iron pyrite FeS_2 is ~ 5.42 Å. The unit cell consists of a face-

centered cubic sublattice of Fe in which S_2 ions are embedded, frequently shown in other MX_2 compounds of transition metals M and chalcogens X = O, S, Se and Te.

Iron atoms are bonded to six sulfur atoms, resulting in a distorted octahedron in which the Fe ions are generally considered to be in the divalent state at low spin (as shown by Mössbauer spectroscopy as well as XPS). The material as a whole behaves like a Van Vleck paramagnet, despite its low spin divalence.

Sulfur centers occur in pairs, described as S_2^{2-}. Sulfur atoms are tetrahedral, being bonded to three iron centers and one other S atom. The symmetry site at the Fe and S positions is represented by the symmetry point groups C3i and C3, respectively. The absence of inversion centers at the S-lattice sites has important consequences for the crystallographic and physical properties of iron pyrite. These consequences arise from the active crystal electric field at the sulfur lattice site, which results in polarization of S ions in the pyrite lattice.

1.1.2 Morphology

According to the shape distinction of different morphologies, FeS_2 nanostructures are divided into 0D, 1D, 2D and 3D. These classifications include dimensionless nanoparticles, nanowires and microspheres, which were synthesized under specific experimental conditions. [9] Such as temperature, Fe and S content of the solution, solvent used, used methods and reaction time.

For zero-dimensional (0D) nanomaterials, all dimensions are measured within the nanoscale (< 100 nm). The most common are dimensionless nanoparticles. For one-dimensional (1D) a nanomaterial, one-dimensional is > 100 nm; this class includes nanotubes, nanorods, and nanowires. In 2D nanomaterials, two-dimensional is > 100 nm. This class has a small plate shape, nanofilms and nanosheets. Three-dimensional nanomaterials (3D) are materials that are not limited to nanoscales in any dimension. This class includes nanowires, nanotubes, and microspheres. [10]

Figure 1.3-6 show the SEM micrographs of different shape morphologies of different nanoparticles type according to experimental synthesis methods.

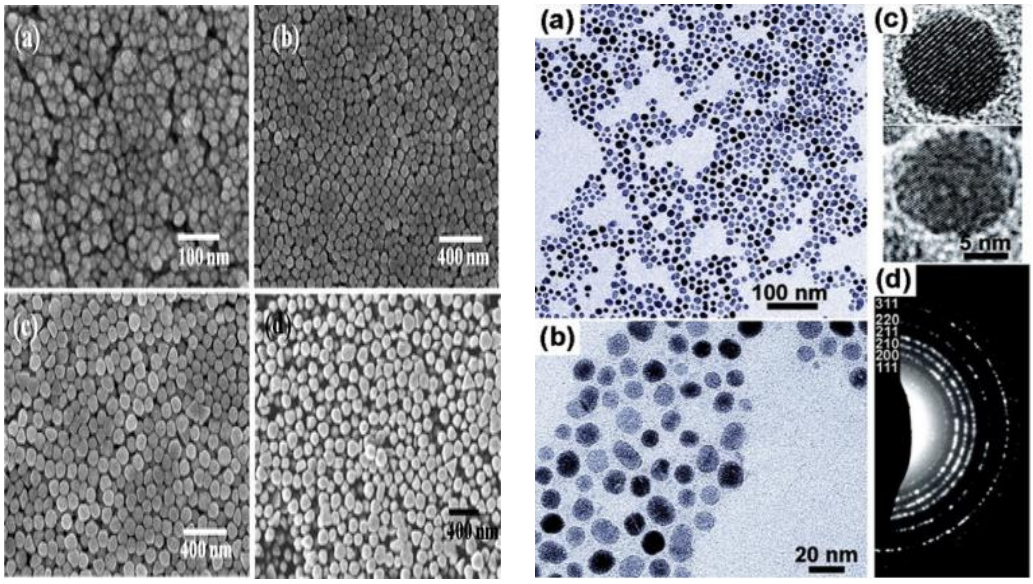

Fig.1.3. TEM, SEM characterization of the colloidal FeS_2 nanocrystals and corresponding films 0D. (a) Low, (b) middle and (c) high magnification TEM images, (d) electron diffraction patterns. [9]

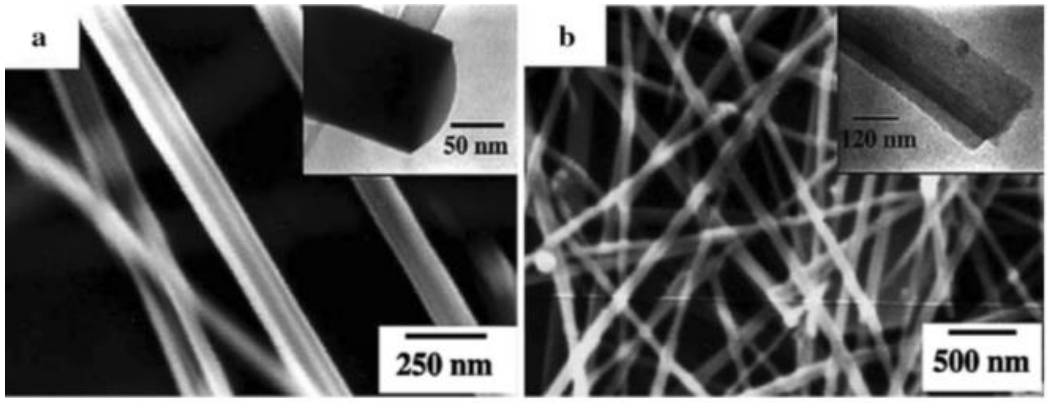

Fig.1.4. SEM images of various 1D FeS_2 nanostructures by controlling iron sources, the molar concentration of precursors and reaction temperature. [9]

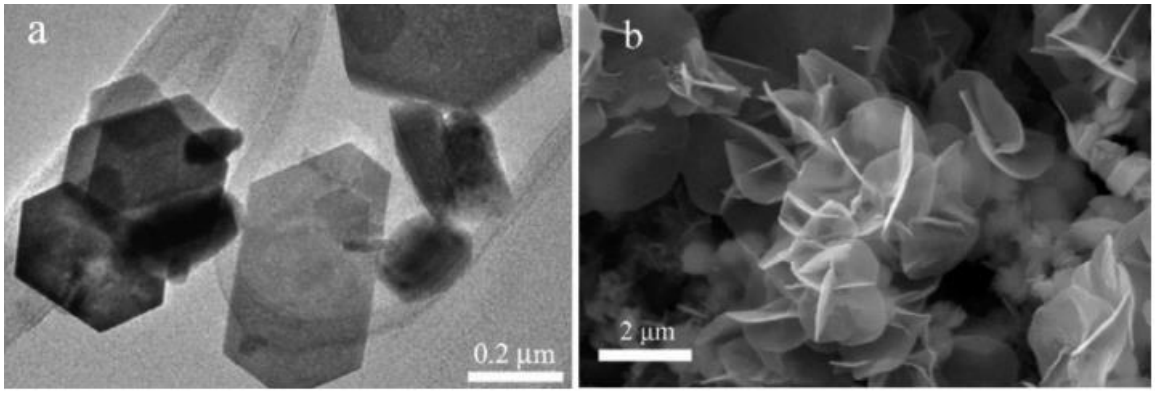

Fig.1.5. SEM images 2D for (a) FeS_2 nanoplates and (b) FeS_2 nanosheets. [9]

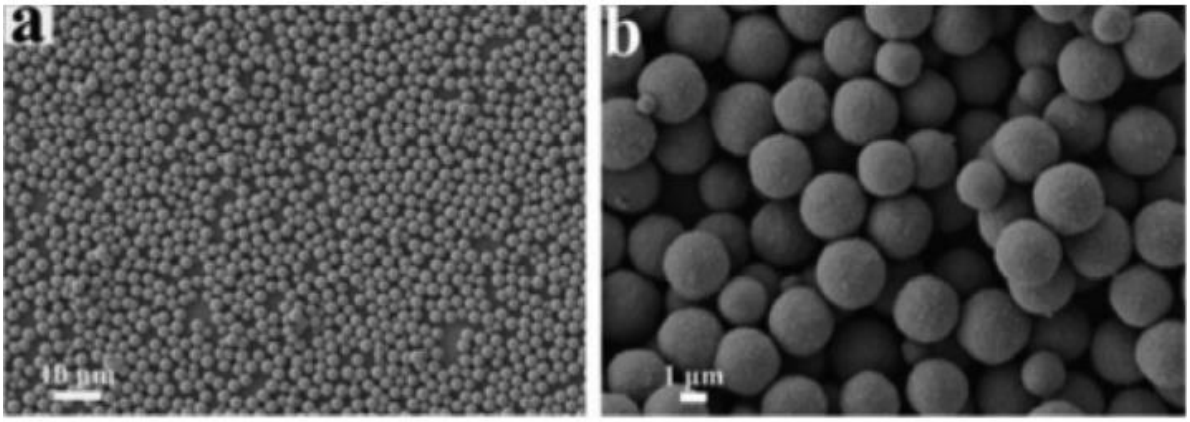

Fig.1.6. SEM images of the FeS_2 3D microspherolites by microwave irradiation (a) low magnification and (b) high magnification. [9]

1.2 Iron disulfide properties

1.2.1 Electronic properties

The basic electronic structure of pyrite has been lavishly studied experimentally and theoretically; many elements are certainly present in the pyrite layers at different concentrations that could affect the electronic properties of the films [7]. Much research has been done on the electronic band structures of the pyrite and marcasite polymorphs of FeS_2.

As we know, FeS_2 is a semiconductor with indirect band gap of 0.95 eV. The maximum and minimum of the valence (VBM) and conduction (CBM) bands are located at the X and Γ-high symmetry points, respectively. Thus, these valence and conduction bands were formed by splitting the 3d orbitals of the Fe atom into two groups. The unoccupied states in the conduction bands are mixtures of Fe_{eg} and $S_{pp\sigma*}$ states, which is crucial for efficient optical absorption. Similarly, the band structure of pure pyrite shows a critical transition of about 1.8 eV located along X-M, which is suitable for many industries. The transition is resulted between the Fe_{t2g} state and the mixed Fe-S (Fe_{eg} + $S_{pp\sigma*}$) state at the X high-symmetry point. The band gap in FeS_2 has been pointed out in various experimental and theoretical works that it can be affected by structural changes.[12]

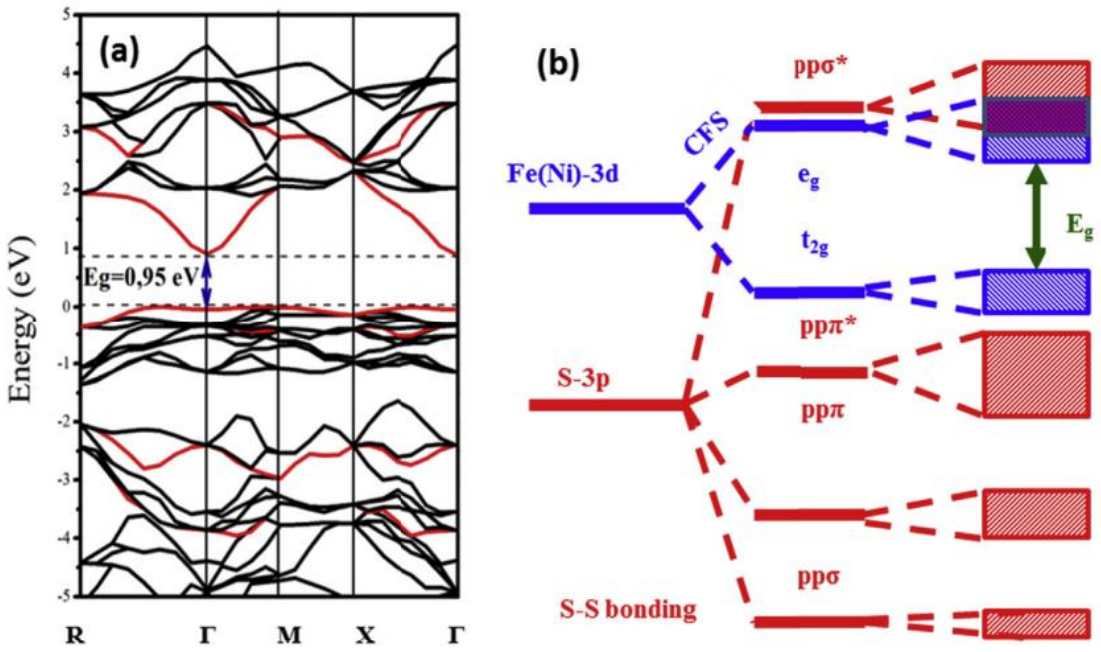

Fig.1.7. Band structure of FeS_2 pyrite obtained by FP-LAPW method. [12]

experimental value 0.95eV and contrasts with the results of Temmerman et al. [12], who obtained 0.64eV, and of Zhoa et al. [13], who obtained 0.59eV. Both these calculated values are less than the experimental value. [11]

In order to improve the band gap doping FeS_2 with Ni was suggested and the value reached 1.24 eV, another Mn doping led to similar results with a band gap of 1.31 eV. In conclusion doping FeS_2 improves carrier mobility introducing commonly filled deep-donor levels. [14]

1.2.2 Electrical properties:

The electrical properties of FeS_2 films on glass and quartz substrates were assessed by variable-temperature, Hall Effect measurements (90–300 ° K) in van der Pauw geometry with thermally deposited, Ohmic silver contacts. The resistivity of pure pyrite films was (1.5 ± 0.5) Ω.cm at room temperature and (30 ± 5) Ω.cm at 90 K (the red trace Fig.8). [7]

Features such as low resistivity, low mobility, and p-type transport have been reported for almost all involuntarily doped pyrite thin films, regardless of fabrication method, which may imply that transport in polycrystalline pyrite films is governed by surface or interface effects rather than bulk properties. The electrical properties of mixed-phase pyrite-marcasite films are almost the same as to those of pure-phase pyrite films. The resistivity at room temperature of the mixed-phase films (blue trace) is only ≈5 times smaller.

The electrical properties of pyrite thin films appear to be independent of S: Fe stoichiometry. This means that the expected donors and acceptors (sulfur and iron vacancies, respectively) do not govern the electrical behavior of the pyrite films.

There are at least three credible explanations for the general electrical behavior of nominally undoped pyrite thin films: phase impurities, accidental oxygen doping, and surface effects.

First, pyrite samples may contain nanoscale inclusions of sulfide metal phases (due to thermodynamic considerations); this idea, recently advocated by Yu et al. [15]. A second possibility is that all pyrite films are contaminated by oxygen and that oxygen acts as an effective acceptor to produce highly doped p-type films. Sun et al. [16] argued that pyrite synthesized under oxidizing, iron-rich conditions can be contaminated with substituted oxygen (Os defects) at a concentration of $\approx 10^{-19}$ cm^{-3} and that the Os impurities are p-type dopants. Third Surface effects provide an explanation for the universal electrical behavior of undoped pyrite films. As argued almost 20 years ago, the similarity of electrical characteristics independent of stoichiometry and preparation method suggests that the electrical behavior of pyrite thin films is determined by surface properties.

Surface and grain boundary effects commonly control the electrical properties of semiconductor thin films via surface nonstoichiometric, oxidation, charge-transfer doping from adsorbed species, inter-grain potential barriers to transport. Given the well-known instability of pyrite surfaces, it is reasonable to expect that surface composition and electronic effects are very important for pyrite thin films and may be responsible for their measured electrical properties. [7]

There may be some regions that alternately have p-type and n-type properties, called p-n-type behavior. It appears that pyrites containing a sulfur deficiency tend to be n-type semiconductors. The n-type can be explained by the excess of Fe atoms with the sulfur deficiency where pyrite becomes a donor; and for the p-type, it is the contrary. So, the pyrite becomes an acceptor when there is an excess of sulfur over the iron deficiency. [17]

The fig 1.9 down below shows the variation in the electrical conductivity of pyrite at 298 °K, based on the data provide by Pridmore and Shuey [18], Schiek et al. [19], and Doyle and Mirza [20]. Based on the whole data set with a number of measurements (n=46), the mean conductivity value is 47.46 $(\Omega cm)^{-1}$ and the median 2.27$(\Omega cm)^{-1}$. Conductivity values range

(0.02-562.32) $(\Omega cm)^{-1}$. There is an obvious difference between the n-type and p-type pyrite conductivities where the n-type shows a higher general conductivity of 56.08 $(\Omega cm)^{-1}$ and a median of 3.32 $(\Omega cm)^{-1}$ (n=39). While the p-type pyrite have a mean conductivity of 0.53 $(\Omega cm)^{-1}$ and the median of 0.09 $(\Omega cm)^{-1}$ (n=7). [17]

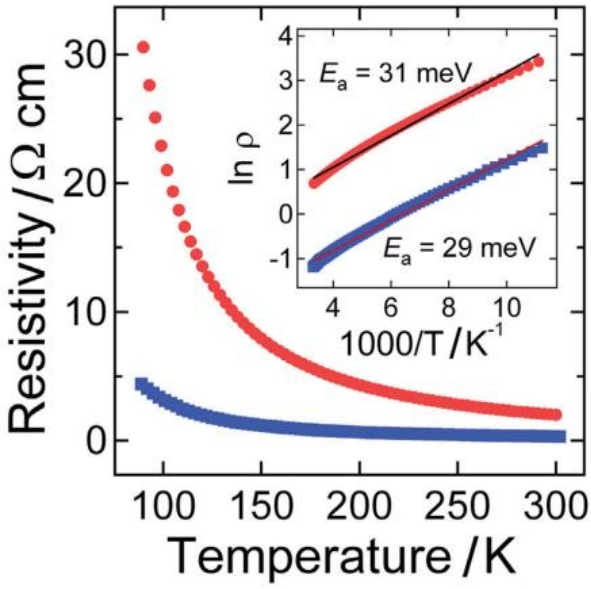

Fig.1.8. Electrical resistivity of pure pyrite and mixed-phase FeS_2 films. [7]

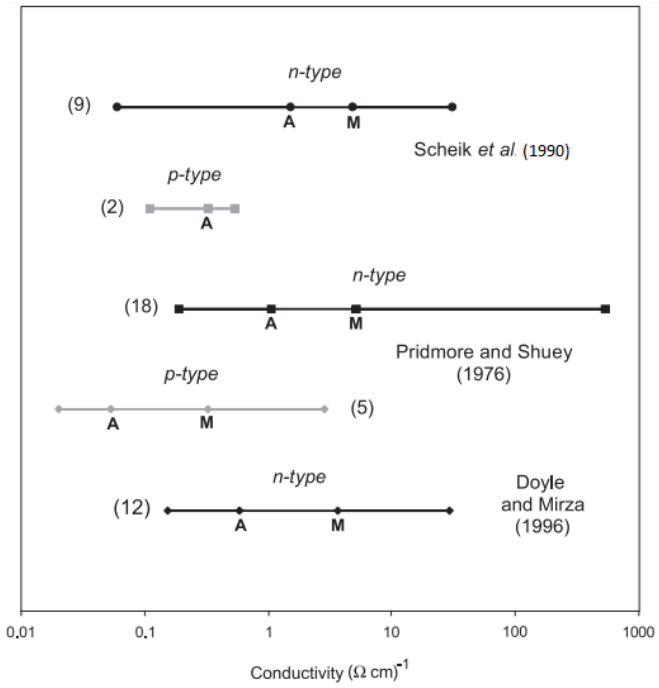

Fig.1.9. Variation in the conductivities of pyrite based on the work of Doyle and Mizra (1996), Pridmore and Shuey (1976) and Schiek et al (1990). (A) Denotes the mean value, (M) denotes the median. The (number between bracket) next to each bar denotes the number of measurements. [17]

1.2.3. Optical and optoelectronic properties:

There is a law called the beer's law or the Beer-Lambert law that defines a relation between the attenuation of light through a substance and the properties of that substance, mathematically expressed as: [21]

$$\ln\left(\frac{I_t}{I_0}\right) = -k_1.d \qquad 1.1$$

According to Beer's law, the light attenuation also depends on the concentration *C* of the attenuating species. Therefore, the decay in the intensity of light can be expressed as:

$$\ln\left(\frac{I_t}{I_0}\right) = -K.d.C \qquad 1.2$$

With k_1 and *K* are the proportionality constants.

"The Absorbance" A of light is expressed as the product of the extinction coefficient ε and concentration C of the attenuating species present, and the optical path length d (thickness). The relationship is expressed as follows:

$$A = \varepsilon.d.C \qquad 1.3$$

From equations 2 and 3, the decay in the intensity of light can be expressed as:

$$I_t = I_0 e^{-A} = I_0 e^{-\varepsilon.d.C} \qquad 1.4$$

Transmittance *T* of light travelling through an absorbing medium is defined as:

$$T = \frac{I_t}{I_0} \qquad 1.5$$

The relationship between the transmittance and absorbance is obtained from equation (3), (4) and (5) as:

$$A = -\ln(T) \qquad 1.6$$

Using the 6th equation, the absorbance coefficient is presented as follows:

$$\alpha = -\frac{dA}{dl}\Big|_{l=0} \qquad 1.7$$

Nowadays, iron pyrite attracts much attention for its ability to boost the solar cells industry. Within the present case and according to the Shockley–Queisser theory, the band

gap of FeS_2 is narrow for photovoltaic applications. Therefore, some of chemical elements can improve the pyrite band gap, namely transition metals; for that reason doping pyrite is a way to adapt the photovoltaic properties [14]

The idea of doping pyrite with a higher gap material was firstly mentioned in the work of Altermatt et al. [22] to investigate absorption coefficient, many different element doping with variable concentrations were considered such as manganese Mn.

Fig.1.10 shows optical absorption coefficient of sample A non-doped FeS_2 and sample B doped FeS_2 with 0.60 (mol/L) of Mn^{2+}. where the absorption coefficient of sample A is 2.0 x 10^5 cm^{-1} and then increased to 3.70 x 10^5 cm^{-1} in sample B. there is an obvious relation between the absorption coefficient and the concentration, and since the concentration of doped Mn affects the microstructures of the films; the absorption coefficient is related to the changes of the grain morphology in these thin films, which can be illustrated in the diagram shown in fig.1.11. [23]

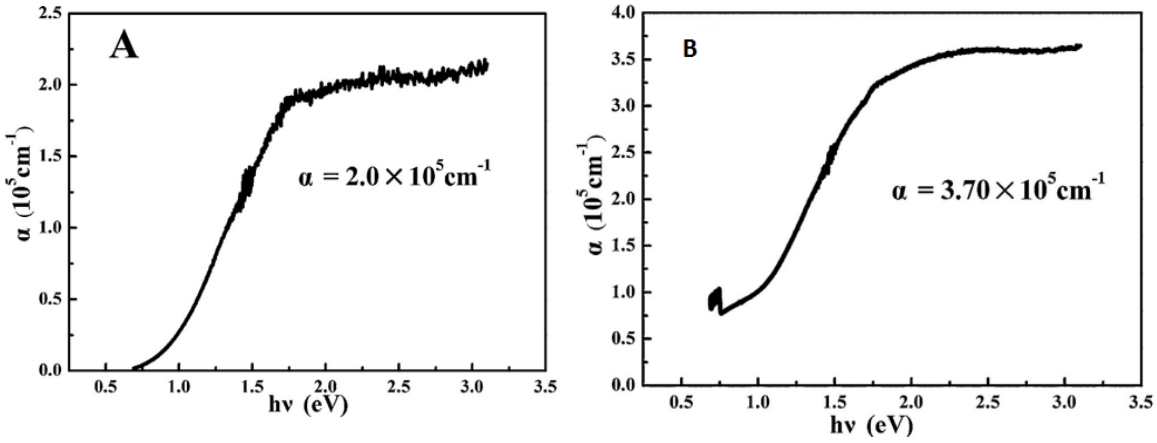

Fig.1.10. Optical absorption coefficients of the films sample with different doping concentrations. [23]

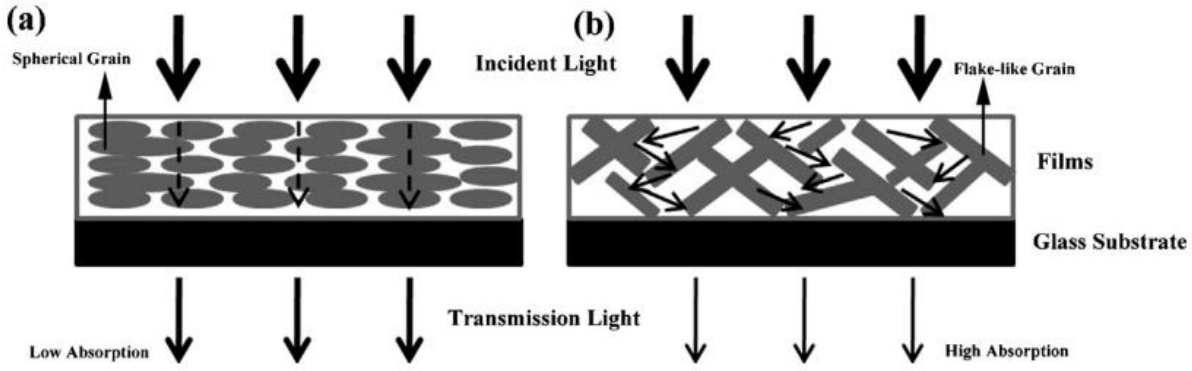

Fig.1.11. Schematic diagrams of the light absorption in films. [23]

Fig.1.11. represent a diagram of the light absorption, in (a) most light is inclined to transmit in a direct way within the internal structures of films, which leads to relatively low absorption. (b) Shows that most of grains are being flaky and bridged with each other continuously forming a light-trapping network allowing the reflection of incident light with many times in the inner films, leading to a strong light absorption. [23]

In another research FeS_2 was doped with copper (Cu) and nickel (Ni) and the same encouraging results were found, there is always an improvement in the material properties. Accordingly doping FeS_2 with transition metals makes a very promising material for energy applications. [24]

1.2.4. Magnetic properties

Pyrite has been reported to have a wide range of magnetic properties [18], and it appears that is non-magnetic due to the weak spin configuration of iron Fe^{2+}. This was explained by Neel and Benoit as follows: 16 valence electrons (8 from Fe and 8 from S2) are redistributed in the FeS_2 molecule, and 10 electrons completely occupy the 3d Fe shell and the 6 Ss the 3p shells [25]. The synthesis of iron disulfide-based thin films can be considered in two-dimensional non-van der Waals (nvdW) systems, which are gaining popularity due to their enormous potential in catalytic and storage applications. Recent research shows that it is good precursor materials for magnetic applications. Calculations predicted that a nano-sheet of FeS_2 at the (111) orientation is stable and can be exfoliated quite easily due to its low exfoliation energy. It consists of a layer of iron atoms sandwiched between two layers of sulfur atoms retaining the crystallinity of the parent pyrite structure, resulting in a ferromagnetic base and anomalous ferromagnetic behavior of the exfoliated pyrite sheets.

Furthermore, it has already been shown that layered manganese-containing sulfides and selenides (MnX2; X=S, Se) with a pyrite-like structure exhibit high-temperature ferromagnetism up to monolayers, whereas their bulk counterparts are antiferromagnetic materials at low temperatures.

In pyrite, the S-Fe-S angle and Fe-S bond length are 113.5° and 2.00 Å, respectively. The total cluster moment is of 4 μ_B results from a parallel magnetic coupling between the iron atom (3.16 μ_B) and the S atoms that are substantially polarized (0.42 μ_B). For the anionic cluster FeS^{-2}, the putative ground state is also a folded structure without the S-S bond. The S-Fe-S angle and Fe-S bond length are increased to 143.8° and 2.09 Å, respectively, compared

to the neutral cluster (113.5°and 2.00 Å). This results in a less compact cluster, an Fe spin moment of 3.80 μ_B and an induced moment on the S atoms of 0.60 μ_B, leading to a total cluster moment of 5 μ_B.

To study the magnetic properties heat must be included because thermal treatment helps the formation of magnetic phases of pyrrhotite and magnetite. The more the temperature increases magnetization of treated pyrite increases as well followed by a magnetic recovery increasement. [26]

The results of the magnetic recovery of pyrite are shown in Fig.12. Initially the recovery in the magnetic fraction is very low and remains so, but once the temperature increases and reaches about 400 C° the magnetic recovery increased to 80%.

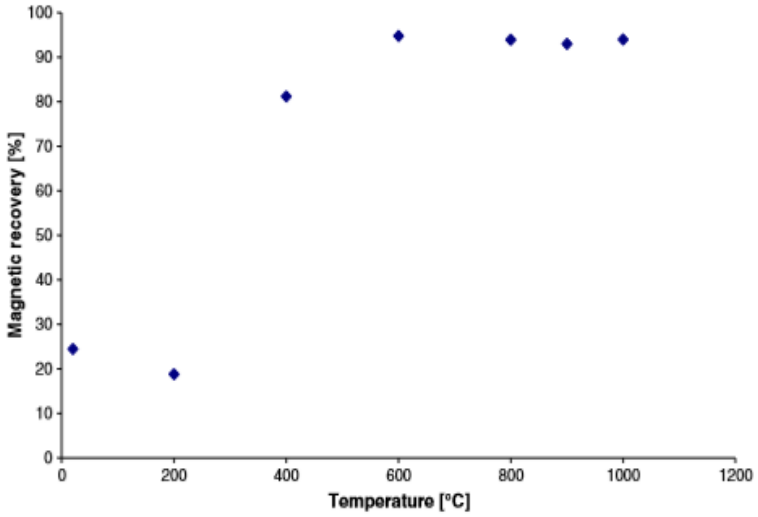

Fig.1.12. Magnetic recovery of the heat treated pyrite. [26]

The heat treatment has a great influence on the magnetic properties of pyrite by increasing the saturation magnetization as more magnetic phases of pyrrhotite and magnetite are formed. At temperatures of 800 ° C, the formation of hematite, which has much weaker magnetic properties, significantly reduced the magnetization. At processing temperatures above 800 ° C, the formation of maghemite increases magnetization yielding to strong magnetic recovery. A recovery of 23% was obtained for the untreated sample, and the maximum recovery after treatment at 600 ° C increased to 94%. [26]

1.2.5. Electrochemical properties

Electrochemical mechanisms have been used for over 50 years to clarify several phenomena in the flotation process such as changes in pyrite surface chemistry due to oxidation, the interaction of pyrite with other components. It has been found that absorption of collectors onto sulfide minerals occurs via an electrochemical mechanism. Therefore, it is considered an important parameter in controlling the recovery and selectivity of sulfide minerals.

The oxidation-reduction environment is very sensitive to iron in galvanic contact. Therefore, investigation has been done on both pyrite and pyrrhotite using different pH values with the respect of the two reference electrodes. [27]

When FeS_2 is completely oxidized, it is converted to iron and sulfate ions. Oxidation of pyrite occurs according to the following reaction:

$$FeS_2 + \frac{7}{2}O_2 + H_2O \leftrightarrow Fe^{2+} + 2SO_4^{2-} + 2H^+ \qquad (1.1)$$

Laboratory observations have shown that the pyrite oxidation reaction is not a complete reaction, but that ferrous and sulfate ions continue to react to produce sulfur and changed it from S_2^{2-} (in pyrite) on the inner surface to S^0 (elemental sulfur that is suitable for electrochemical reactions) on the external surface. The surface sulfur layer remains associated with the sulfide lattice and the ferrous iron produced:

$$Fe^{3+} + 3H_2O \leftrightarrow Fe(OH)_3 + 3H^+ \quad (1.2)$$

The iron hydroxide produced by chemical reaction (2) precipitates on the mineral surface as a coating, preventing further oxidation of pyrite.

The oxidation of pyrite, which produces ferrous iron and sulfate ions, results in the loss of seven electrons from each sulfur atom. Because one or two electrons are transferred in each reaction, the oxidation process is complex and involves several steps. The most important one is to break the strong bond between iron and sulfur then forms thiosulfate ions as intermediates:

$$FeS_2 + 1.5O_2 \leftrightarrow Fe^{2+} + S_2O_3^{2-} \qquad (1.3)$$

The high open circuit potential of pyrite is due to the strong bond between iron and sulfur in the pyrite lattice. In the pyrite electrode potential vs time plot (V (t)), see Fig.13. It can be observed that the potential increases over time until it reaches steady state. The relationship between potential and pH is proportionally inversed. The reason for this increase can be explained by the production of sulfate at several stages. That is, at each reaction stage, the potential increases by a defined amount until the maximum limit and steady state are reached. The electrochemical reaction occurs at higher rate intensity and at a lower pH value, increasing the intensity of the electrochemical reaction removes hydrophobic species from the surface of the mineral, and the high open circuit potential allows pyrite acts as a cathode for galvanic contacts. [27]

After a lot of other researches, they discovered that cubic FeS_2 has interesting and promising electrochemical properties such as delivering a large discharge capacity, which probably will help future applications as an electrode material for lithium cells, cathode for rechargeable batteries. [28], processes like refining fuels and purification of gas wastes...

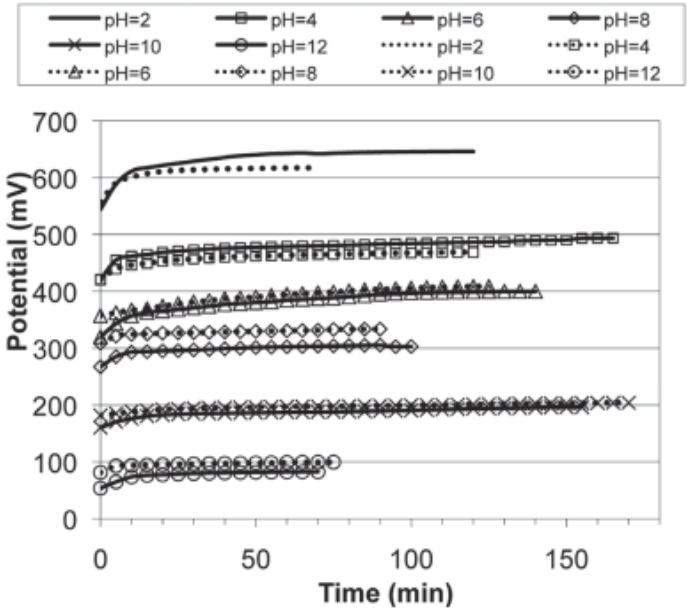

Fig.1.13. Time-potential relationships of pyrite with respect to saturated calomel reference electrode (solid line) and to gold reference electrode (dotted line). [28]

Pyrite FeS_2 can be used in CO_2 reduction to produce methanol CH_3OH, a future energy carrier, and a significant chemical compound. It has been found that FeS_2/NiS solvothermally made nano composite of 14 nm diameter confirms high specific surface area and gradual

active sites, which effectively improve the catalysis activity; it performs high FE (Faraday efficiency) of 64% at -0.6 V and a stable current density of 3.1 $mA.cm^{-2}$ over the 4 hours stability test and there is no obvious degradation. The result is due to the formed active sites between FeS_2 and NiS shown in Fig.14. FeS_2/NiS nano composite exhibits excellent activity toward CO_2 reduction compared to nano crystals of FeS_2, NiS and the physical mixture of FeS_2 with NiS. [3]

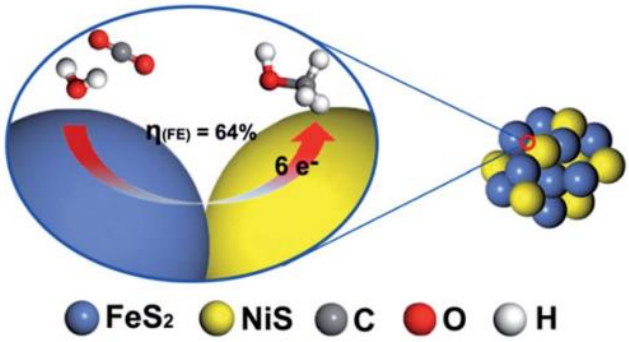

Fig.1.14. The proposed reaction mechanism of electroreduction CO_2 by FeS_2/NiS nanocomposite electrocatalyst). [3]

1.2.6. Photoluminescence and thermoluminescence properties

Photoluminescence is a luminescence phenomenon, it is the optical radiation emitted by a physical system, resulting from excitation to a nonequilibrium state by irradiation with light. Three processes can be distinguished:

(1) Creation of electron-hole pairs by absorption of the exciting light.
(2) Radiative recombination of electron-hole pairs.
(3) Escape of the recombination radiation from the sample.

Since the exciting light is absorbed in creating electron-hole pairs, the greatest excitation of the sample is near the surface. [29]

Since PLs occur near the surface of the material, their analysis is a powerful tool for obtaining discrete electronic states and many other parameters near surfaces, interfaces, crystal damage and a high surface quality. Once the signal of PL is detected it tends to be utilized to characterize both radiative and non-radiative mechanisms. [30,31]

Pure FeS_2 nanosphere morphology was synthesized by a solvothermal method, an alternative to colloidal synthesis, to obtain nanaopheres averaging ~ 50 nm diameters with a smooth surface; the photoluminescence was measured by micro-PL at 77K and UV–vis–NIR

(ultra violet visible near infrared) spectrophotometer as shown in Fig.15. The high intensity peaks is sharp and narrow centered at 892 nm with a band gap of 1.39 eV. It is well consistent with UV-Vis results.[31]

Nanospheres consistently show good visible absorption range and are considered excellent solar absorbers. Additionally PL intensity is widely regarded as indicator of high quality surface. [31]

Thermoluminescence (TL) is a semiconductor luminescence phenomenon that can be observed when a solid is thermally excited. At higher temperatures, the solid emits infrared light, its intensity increases as the temperature rises. TL in other meaning is heat stimulated emission after pre-absorbing radiant energy; three essential processes must be done to produce TL [32]:

(1) The material must be a semiconductor (metals do not have luminescent properties);
(2) The material must have, at some point, absorbed energy during exposure to ionizing radiation;
(3) The luminescence emission is stimulated by heating the material.

TL theory, commonly referred to as TL kinetics has been concerned with the shape, temperature at maximum peak (Tmax) and kinetic parameters of single peak glow curves that's why Thermoluminescence of pyrite has been explored. The material used frequently has one large and four small peaks. Up on a closer examination, the glow curve of a single natural pyrite crystal sample contains two low-intensity thermoluminescence (TL) peaks at 90°C and 165°C. The general one trap (GOT) kinetic equation was used to derive what is currently called the 1st and 2nd order kinetic equations. [33]

The GOT equation describing the trapped charge concentration is:

$$-\frac{dn}{dt} = nse^{-E/kT}\left[1 - \frac{\sigma_t(N-n)}{\sigma_r n + \sigma_t(N-n)}\right] \qquad (1.8)$$

1st order kinetic equation is a special case where $\sigma_t = 0$:

$$-\frac{dn}{dt} = nse^{-E/kT} \qquad (1.9)$$

2nd order kinetic equationis reduced if $\sigma_t = \sigma_r$:

$$-\frac{dn}{dt} = n^2 \left(\frac{s}{N}\right) e^{-E/kT} \qquad (1.10)$$

These equations provide information on temperature of the glow peak maximum (Tmax) for different doses n_0.

Glow curves were obtained by heating samples consisting of natural pyrite (FeS_2) crystals that were broken into chips and powder with a grain size of ≤ 0.5 mm on a tantalum strip in a Helium-filled chamber and temperatures are determined from chrome1-alumel thermocouples welded to the bottom of the heating strip. To obtain a precise linear heating rate, the thermocouple output is compared to a linear ramp signal; all glow curves analyzed result from a four step process:

2. First, a "data" curve was recorded by heating the sample from 40° to 450° C ;
3. The sample was cooled to below 40° C, and without opening the chamber or changing the atmosphere ;
4. The oven glow was subtracted from the data curve to obtain the TL emission ;
5. The difference curve was normalized to a 5 mg sample mass.

Irradiation and heating do not significantly alter the TL properties of the samples even though there are changes in the surface and magnetic properties.

This is well illustrated by Fig.16 which shows two glow curves obtained with the same sample after doses of 5 x 10^2 Gy. However, between the first (solid line) and second measurement (dashed line), the sample was heated to 450°C four times and received a total dose of ~ 16 kGy; the two curves do not differ significantly. [33]

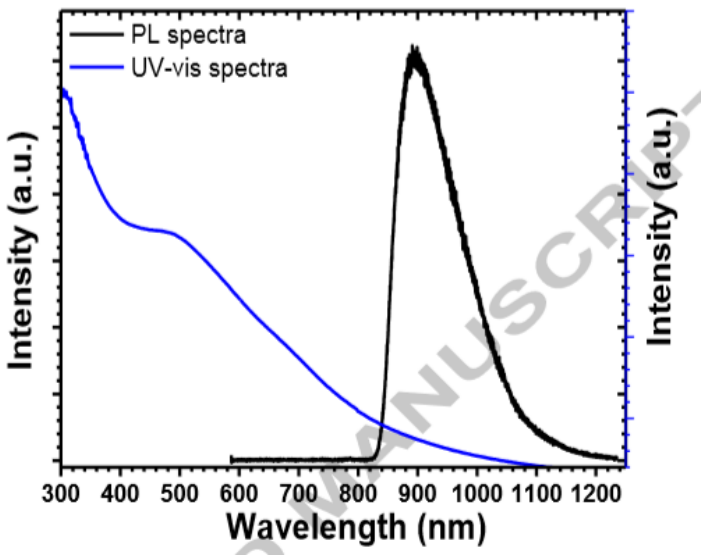

Fig.1.15. UV-Vis spectra and micro photoluminescence (PL) analysis of the nanospheres synthesized, by colloidal route in the ethylenediamine. [31]

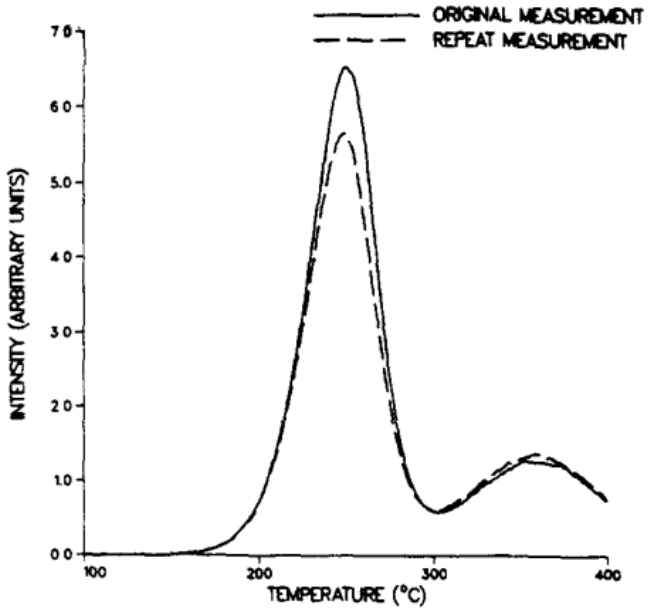

Fig.1.16. The 5 x 10^2 Gy glow curve (solid line) and glow curve (dashed line) from the same sample irradiated to the same dose after it had previously been irradiated to a total of ~ 16 kGy during four successive TL measurements. [16]

1.2.7. Thermoelectric properties

Thermoelectric materials are considered to be very promising for high-temperature power generation application, especially for harvesting waste heat, for onboard power for deep space missions, perfect to solve energy crisis and also it is useful in smart sensors and

refrigerators. A good thermoelectric can convert heat directly into electrical energy with a reasonable efficiency. [34, 36]

The thermoelectric properties are quite sensitive to the details of the band structure, which is why marcasite can be used for low-temperature thermoelectric applications and pyrite can be used for the high-temperature applications.

As it is known, a temperature difference due to a voltage variation is called the Seebeck effect, and in opposite side, it can be called the Peltier effect. The quality of the thermoelectric material is measured by a factor called figure of merit (ZT) with an expression:

$$ZT = \frac{\sigma S^2}{K} T \quad (1.11)$$

Where K, σ, T, S, are respectively, the thermal conductivity, the electrical conductivity, the temperature and the Seebeck coefficient [35] known as:

$$S = \frac{\Delta V}{\Delta T} \quad (1.12)$$

Also σS^2 is known as the power factor PF with an important role to achieve the high efficiency of the materials because it is proportional to ZT [36].

The thermoelectric properties of pyrite and marcasite were investigated using holes-doping leading to the calculated Seebeck coefficient and the power factor PF, which are a function of hole-doping concentrations at different temperatures, as depicted in Fig.17

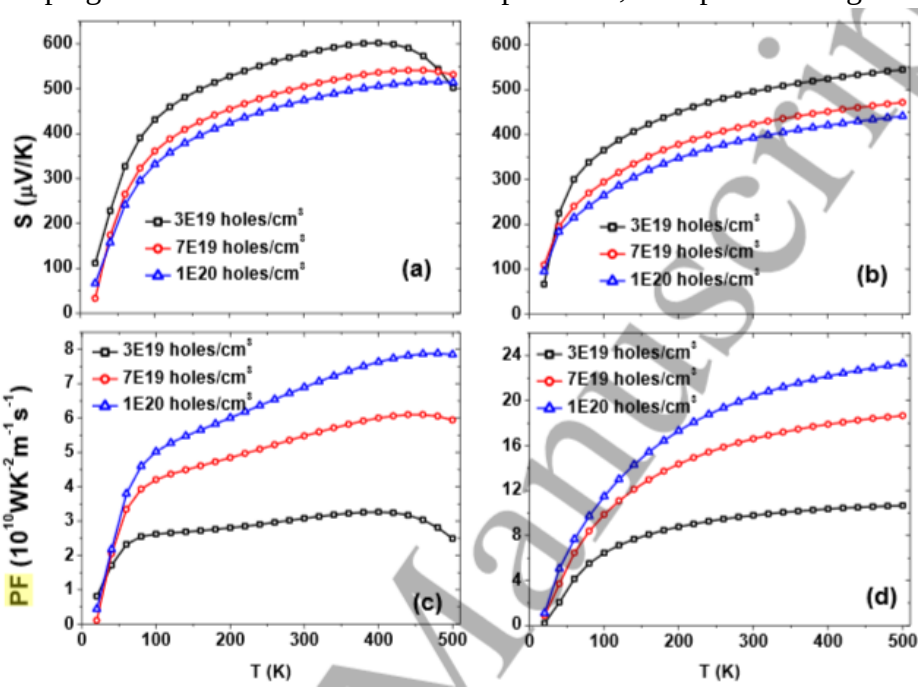

Fig.1.17. Seebeck coefficient for (a) pyrite, (b) marcasite; power factors for (c) pyrite and (d) marcasite as function of temperature at different hole concentrations [36]

As shown in Figs.17a - 17b and for low hole-doping concentrations, S increases exponentially with increasing temperature for both structures. The S of p-FeS_2 varies between (310 – 567) μV/K for the T (100−420)° K and for m-FeS_2, the S increases between (321−501) μV/K for T (100−500)° K; the difference between the S values may be due to the differences in effective masses of the carriers near the Fermi level of both structures.

The larger value of S is expected to lead to a larger PF. This expectation can be checked in Figure 17c and 17d who shows that the PF increases with T and hole concentration n (proportional). It reaches the maximum values of $7.9 \times 10^{10}\, WK^{-2}m^{-1}s^{-1}$ at 480) K for p-FeS2, and $23.4 \times 10^{10}\, WK^{-2}m^{-1}s^{-1}$ at 500) ° K for mFeS_2 structure.

The results indicate that, FeS_2 compound especially the marcasite phase is a promising thermoelectric material with at low temperature hole-doping. The calculation of n-type doping is compared to p-type doping in both structures at T-range 100−500 °K, so it was found that the hole-doping is preferred over electron doping. [36]

1.2.8. Elastic properties:

The elastic properties of a mineral are important because they can provide valuable information about its structural stability, for the elastic properties of pyrite, many experimental and theoretical studies have been undertaken. Two main experimental methods have been followed: X-ray diffraction and ultrasonic methods. [37]

The material is said to be elastic if it returns to its original unload size when unloading and each material has its own elastic limits shown in hook's law:

$$\frac{\text{stress}}{\text{strain}} = \text{constant} \qquad (1.13)$$

Where this constant is given the symbol E and named the modulus of elasticity or Young's modulus. [38]

$$C_{ij} = E = \frac{stress}{strain} = \frac{\sigma}{\varepsilon} \qquad (1.14)$$

Elastic constants are the fundamental material parameters that describe the resistance of the material against applied mechanical deformation. In the case of a cubic system (pyrite) there are only three independent elastic constants [C_{11}, C_{22} and C_{44}]; for an orthorhombic system (marcasite), the number of independent elastic constants increases to

nine [C_{11}, C_{22}, C_{33}, C_{44}, C_{55}, C_{66}, C_{12}, C_{13} and C_{23}]. While , C_{11}, C_{22}, C_{33} represents the elasticity in length which can change with longitudinal strain, and C_{44}, C_{55}, C_{66}, C_{12}, C_{13}, C_{23} are related to the elasticity in shape. [37]

Table.1. sum up calculated constants for pyrite and marcasite at different pressure and show how the elastic constants change with; the elastic constants C_{11} and C_{12} of pyrite raise with increasing pressure, C_{44} also increases but reach a steady rate when P=100 GPa. These results for pyrite are in good agreement with previous studies. For marcasite, C_{11}, C_{22}, C_{33}, C_{12}, C_{13}, and C_{23} are susceptible to pressure; C_{55} and C_{66} have a moderate increase, whereas the elastic constant C_{44} remains almost invariant with increasing pressure. Furthermore, it can be seen that $C_{22} > C_{33} > C_{11}$ over the whole range of pressure, which implies that the atomic bonds along the {0 1 0} planes between nearest neighbors are the strongest, and the atomic bonds along the {0 0 1} planes are stronger than those along the {1 0 0} plane. The elastic constants C_{12} and C_{23} are almost the same, and the difference between C_{55} and C_{66} is very small over the whole range of pressures, which indicates that the difference of elastic prosperities in those directions is small.

Table.1.1. Calculated elastic constants of FeS_2 at various

P(GPa)	Pyrite			Marcasite								
	C_{11}	C_{22}	C_{44}	C_{11}	C_{22}	C_{33}	C_{44}	C_{55}	C_{66}	C_{12}	C_{13}	C_{23}
0	395	119	30	266	387	313	106	165	149	12	87	20
20	580	159	78	406	591	435	129	212	199	85	184	94
40	731	179	120	505	746	537	147	256	242	149	268	153
60	877	192	174	591	882	626	154	289	269	209	352	212
80	988	209	231	671	999	707	161	312	297	273	425	276
100	1094	217	291	744	1085	783	161	337	317	318	511	336
120	1192	223	343	794	1182	848	162	358	336	381	570	392
140	1283	222	411	844	1256	926	164	380	352	433	645	454
160	1369	224	469	886	1345	1005	161	396	370	477	705	513
180	1451	225	531	923	1438	1069	162	409	385	539	769	562
200	1533	226	583	959	1584	1130	163	420	398	608	838	630

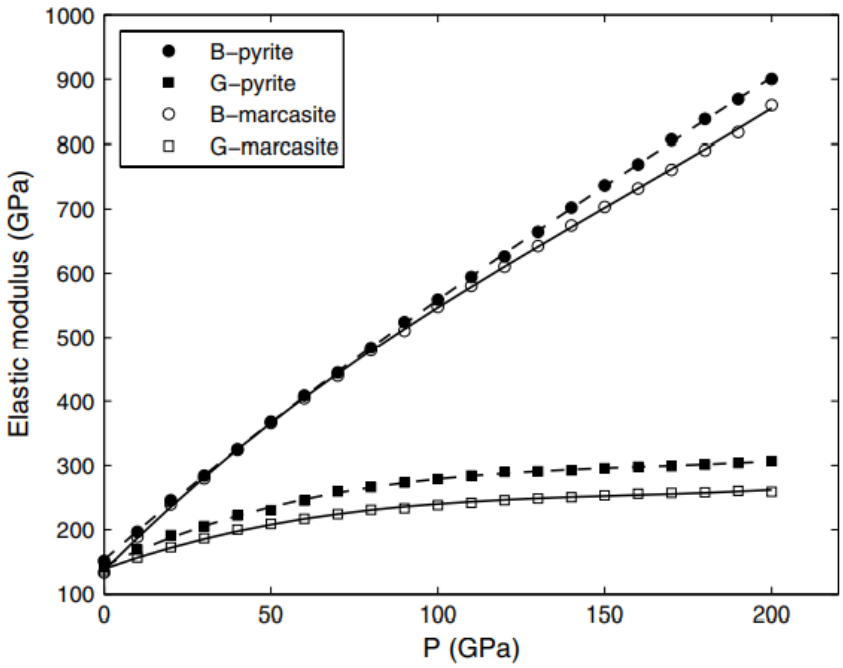

Fig.1.18. Elastic modulus of FeS_2 as a function of pressure [37]

The calculated elastic modulus of pyrite and marcasite is shown in Fig. 18 as a function of pressure from 0 to 200 GPa. The bulk modulus of the two phases is sensitive to pressure, and they are almost the same when pressure is lower than 100 GPa. The shear modulus of the two phases has a moderate increase, and they level off when pressure increases to 100 GPa. According to the table and the fig, we know that the ratio of bulk modulus to C44 increases with increasing pressure; thus, it is liable to shear transformation at high pressure. We find that the pyrite is stable over the range of 0–200 GPa, but marcasite is unstable for pressure up to 130 GPa, which indicates that it may undergo a structural phase transition at 5.4 GPa. [37]

Chapter 2:

2.1. Introduction

FeS_2, which has abundant nanostructures such as nanoparticles, nanowires, nanofilms, and microsferrites, is synthesized under specific experimental conditions depending on the shape difference. [9]

Nanoparticles are of scientific interest because they represent a bridge between bulk materials and atomic and molecular structures. Bulk materials have constant physical properties regardless of their size, but size-dependent properties are observed on the nanoscale. The interesting and unexpected properties of nanoparticles are due to their large surface area.

Creating structures on the nanometer scale gives you control without changing the basic properties of the material, such as melting temperature, magnetic properties, charge capacity, and even color without changing chemical composition; This potential will help achieve new top performance Products and technologies that were previously impossible. [39]

Thin film deposition can be divided into three groups based on the type of deposition. However, this classification was done considering the physical or chemical processes involved. [40]

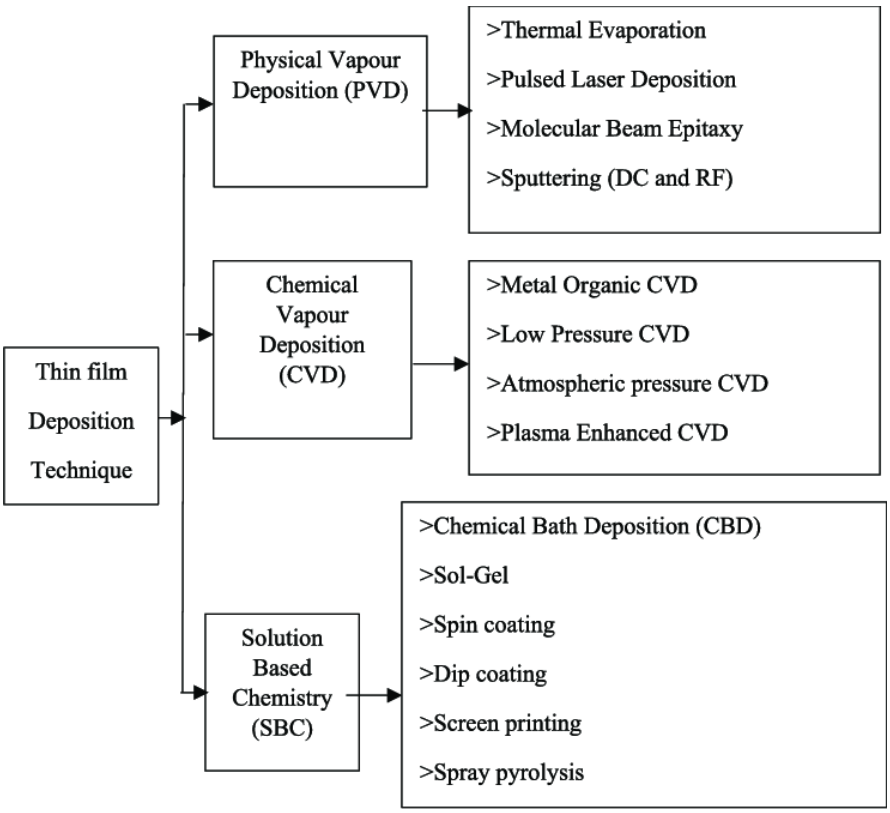

Fig.2.1 Classification of thin film deposition methods. [40]

2.2. Thin film deposition techniques

2.2.1. Solution based chemistry (SBC) process

a. Sol-gel (solution-gelling)

Sol-gel is a process for making solid materials from small molecules. In this chemical process, the sol (or solution) gradually evolves to form a gel-like biphasic system containing both liquid and solid phases, morphology ranging from discrete particles to continuous polymer networks. [41] The general procedure for synthesizing metal nanoparticles can be divided into five stages as follows: [42]

- Hydrolysis
- Condensation (gelation).
- gel aging
- applications
- curing

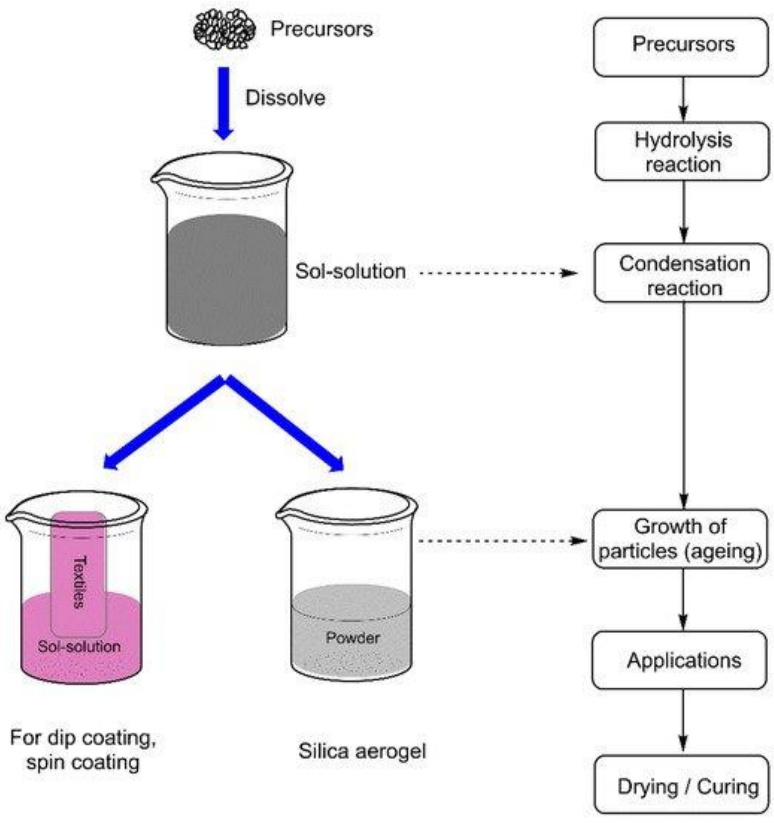

Fig2.2 Steps involved in a sol-gel process. [42]

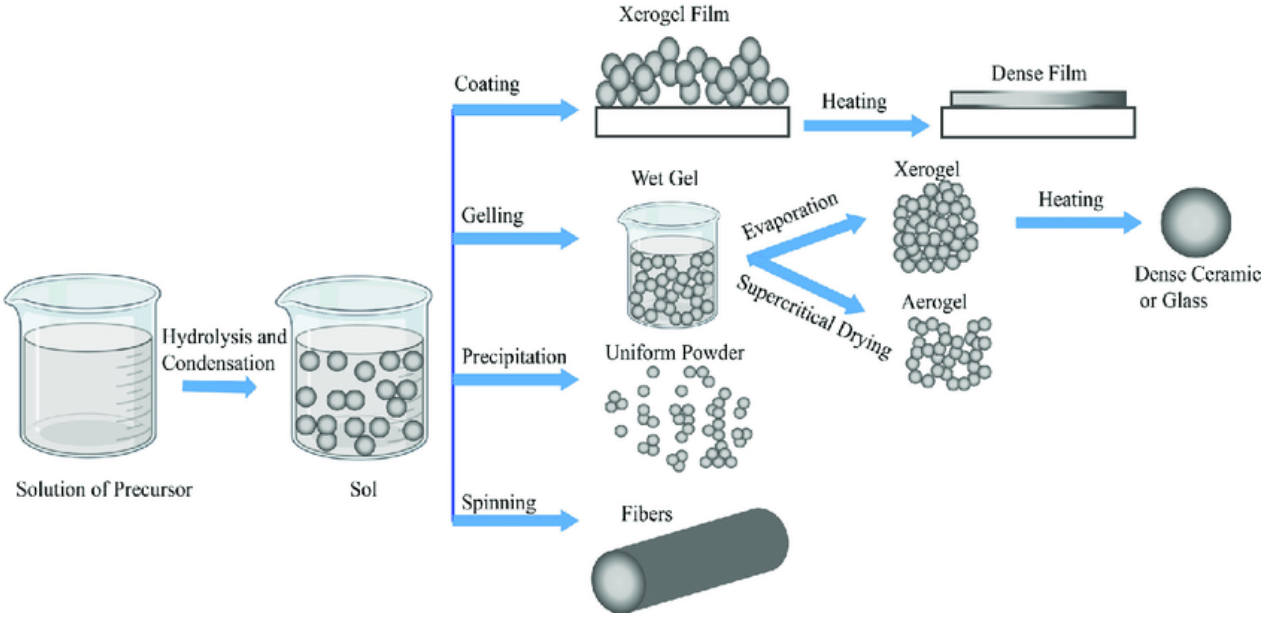

Fig.2.3 Different sol-gel process steps to control the final morphology of the product. [42]

b. Chemical Bath Deposition Technique

Chemical bath deposition techniques were widely used for the deposition of sulfide, selenids, and oxides... The choice of this method results from low cost, easy handling, possibility of application to large surface area, and simplicity of equipment for deposition. This technique allows control of film thickness and chemical composition by varying deposition parameters such as temperature, precursor concentration, complexing agent used, and solution pH. This method relies on the deposition of thin films from aqueous solution, either by current flow or by a chemical reaction under appropriate conditions. With proper control of deposition parameters, a definite composition of the thin film can be obtained.

In CBD process, thin films are deposited on a solid substrate when it is immersed into a dilute solutions of one or more metal salts (MP+), a source of chalcogenide, X (X=S, Se, Te) ion and a suitable complexing agent in an aqueous solution. Using this method, a metallic chalcogenide film is formed on the substrate in four steps: [43]

- Establishment of equilibrium between water and the complexing agent

- Formation of metal- complex species

- Hydrolysis of the chalcogenide source

- Formation of the solid film on the substrate

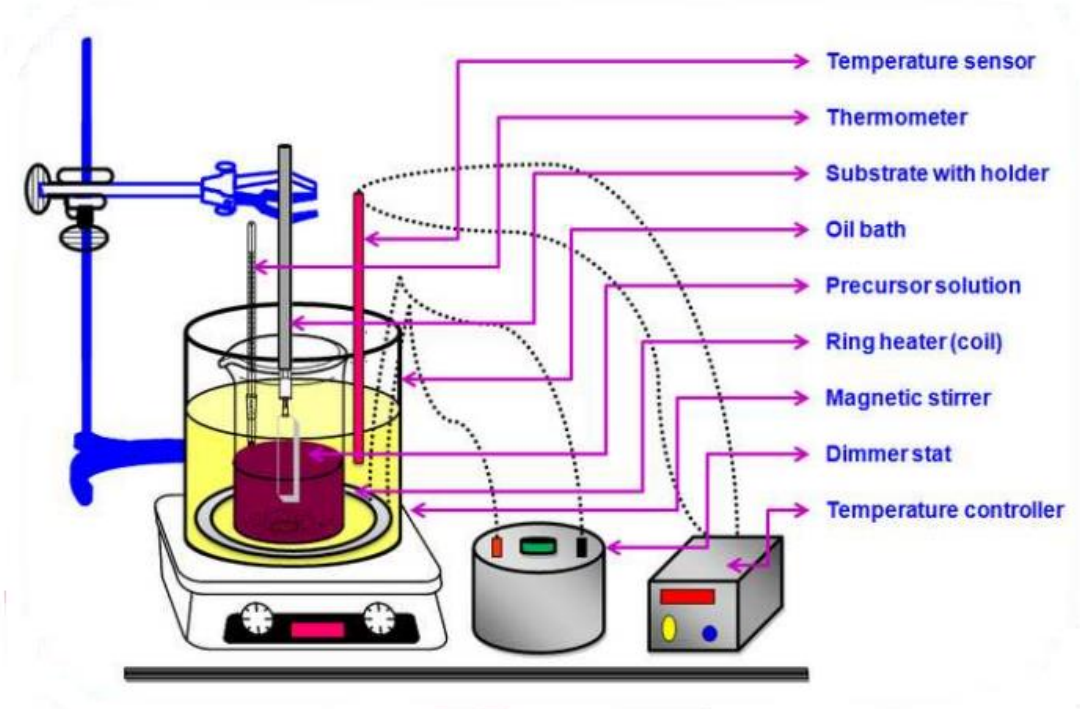

Fig.2.4 Experimental setup for chemical bath deposition of thin film. [43]

c. Spray pyrolysis

Spray pyrolysis is the process of depositing a thin film by spraying a solution onto a heated surface, where the components react to form a compound.

The chemical reaction is selected so that the product other than the desired compound is volatile at the deposition temperature. This process is particularly suitable for oxide deposition and has long been used as a manufacturing process for applying transparent conductors made of SnOx to glass. [44]

There are two different processes, the droplet resides on the surface as the solvent evaporates, leaving behind a solid that may further react in the dry state. Or, the solvent evaporates before the droplet reaches the surface and the dry solid impinges on the surface, where decomposition occurs.

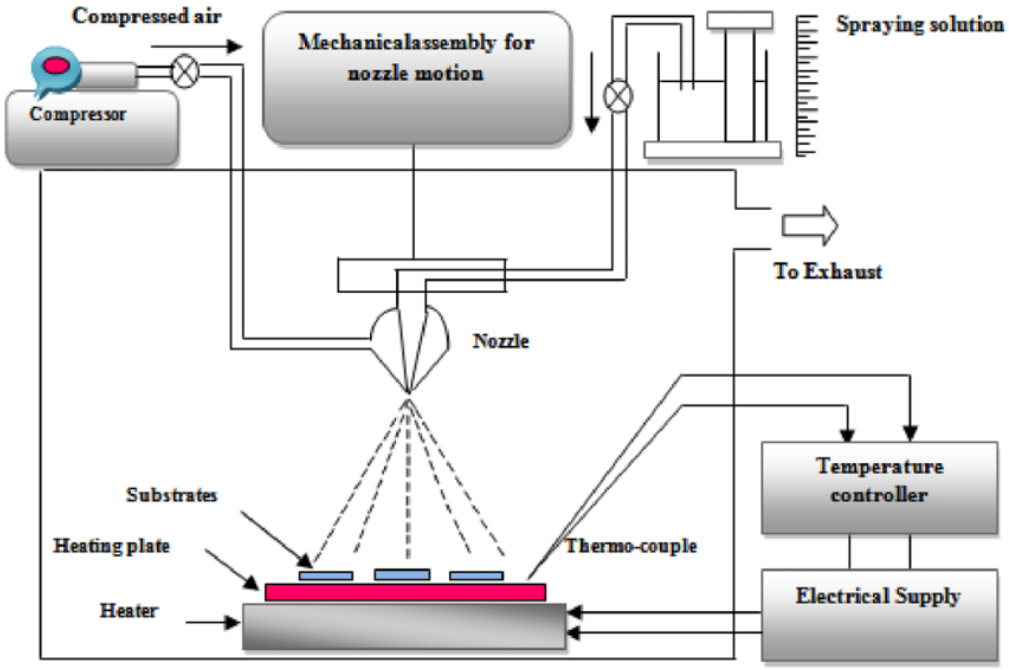

Fig.2.5. Spray pyrolysis system. [44]

d. Spin coating:

Spin coating is a method of applying a uniform film to a solid surface using centrifugal force, and requires a gas-liquid interface. The typical procedure is to place the liquid in the center of a circular surface and rotate it rapidly to produce a uniform film with a thickness of 1-10 μm. The centrifugal force of rotation causes the liquid to spread over the film and cover the surface. [45]

This process can be broadly divided into four main steps: Deposition, spin up, spin off and evaporation.

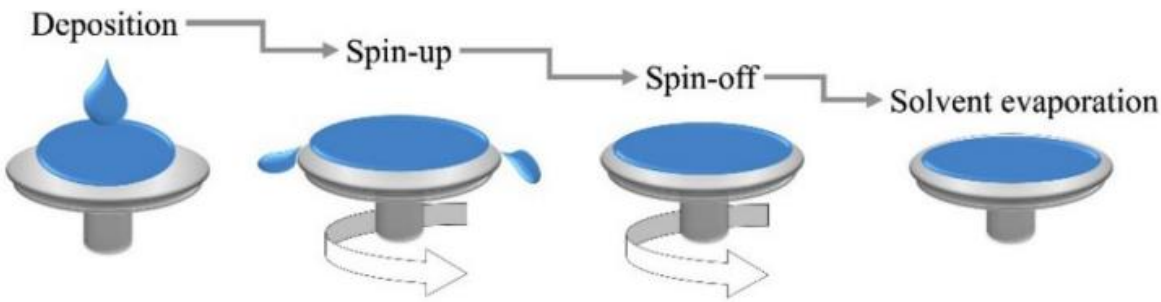

Fig.2.6. Schematic diagram of thin film formation in spin-coating method. [45]

e. Dip coating

In addition to the above techniques, there is another very simple, inexpensive, reliable and reproducible coating process called dip coating. It is a simple process that deposits a wet liquid film by immersing the substrate in a solution containing hydrolyzable metal compounds (or easily formed particles) and pulling them out at a constant speed into an atmosphere containing water vapor. After removing the substrate from the solution, a uniform liquid film is formed on the substrate surface and after drying at room temperature, the volatile solvent is removed, a chemical reaction takes place and the coating film becomes thin. [46]

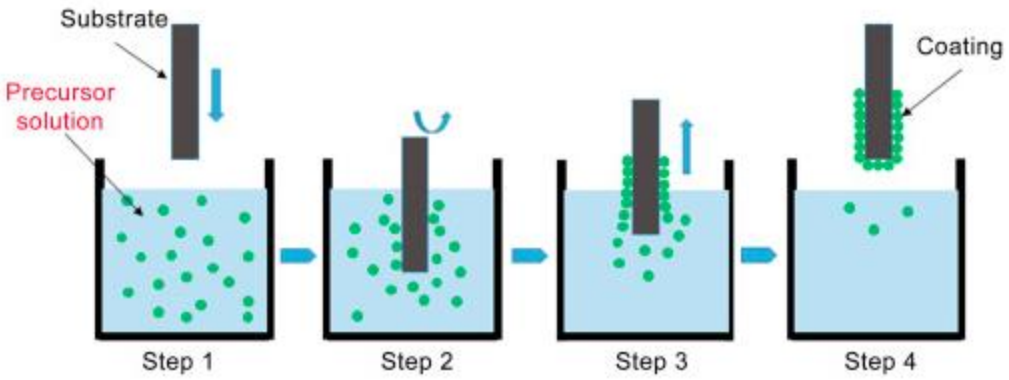

Fig.2.7. Representation of dip-coating technique. [46]

2.2.2. Chemical vapor deposition (CVD) process

CVD is a process for thin film deposition by a series of chemical reactions under specific conditions such as temperature, pressure, reaction rates… The process of material synthesis occurs when the vapor phase component of the target reacts near or on the surface of the substrate through a chemical process, resulting in the growth of a thin film.

A CVD process is typically characterized by volatile between by-products and unused precursor species. Many CVD reaction by-products are very dangerous such as H2, Cl2, HCl, HF, or water vapor. Appropriate safety measures are required when using this process and Flushing of vents, by-products, and unreacted compounds is essential in the process. CVD can be grouped based on the energy used to facilitate a chemical reaction; this energy source is a photon, a laser or temperature (heat). [44]

CVD contains variable processes like, metal organic CVD, low pressure CVD, atmospheric pressure CVD and plasma enhanced CVD.

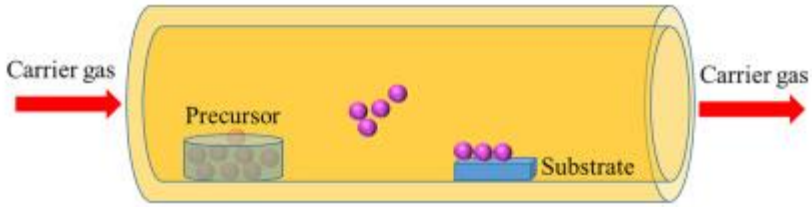

Fig.2.8. Chemical vapor deposition process. [44]

2.2.3. Physical vapor deposition (PVD) process

a. Pulsed laser deposition:

Pulsed-laser deposition is a thin film synthesis technique that uses high-energy laser pulses on the order of nanoseconds to ablate the target material. The laser emission focuses on the surface of the target, absorbs the material and evaporates rapidly, resulting in the ablation of the atoms, which are then collected on the substrate. Since the energy source (laser) is outside the vacuum chamber, this method has the advantage that it can be performed under ultra-high vacuum or a wide range of ambient pressures and gas types. The target is typically rotated so that the same stains are not removed repeatedly. [47]

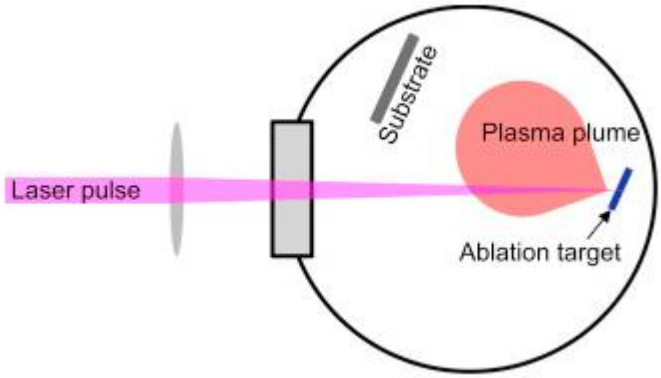

Fig.2.9. Pulse laser deposition process. [47]

b. Sputtering deposition process:

Sputtering is one of the most important PVD techniques in which the physical vaporization of atoms from the surface is caused by the momentum transfer from bombarding, energetic, and atomic-sized particles. Sputter vapor deposition improves composition control of multi-element films and increases flexibility in the types of materials that can be deposited. It operates on two principles: DC and high frequency sputtering systems. [48]

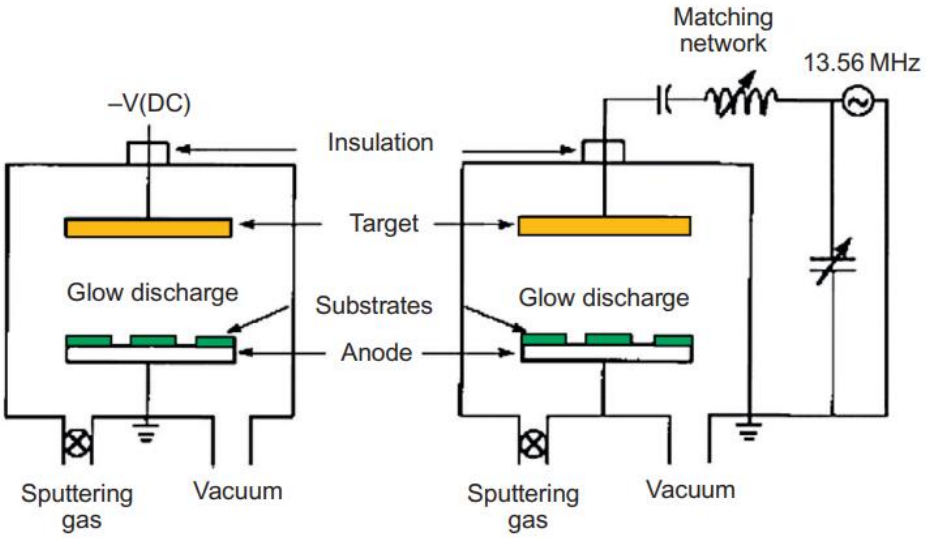

Fig.2.10. Schematic diagram of the principles of (A) direct current (DC) and (B) radio-frequency sputtering systems. [48]

c. Thermal evaporation deposition process

Thermal (or vacuum) evaporation is an ancient deposition process used to form and grow thin films on the surface of solid materials. This method remains advantageous even in modern environments and has wide applicability for thin film deposition in laboratories and industry [39] and it is Very successful and versatile in the production of nanobelts and nanowires with various properties. [49]

The basic continuous steps of thermal evaporation or vacuum evaporation are: Produced steam by exposing the target material to very high temperatures by sublimation or boiling; after that the vapor released from the target material is transported to the substrate by vacuum and finally vapor condensation occurs forming a solid thin film on the surface of the substrate, and further reproducibility of the deposition cycle leads to thin film growth and nucleation.

This process is often performed at high vacuum pressure (HV), and the trajectory of the target material's movement to the substrate is a linear path trajectory called the line of sight; the steam flow is created by heating the surface of the raw material to a sufficiently high temperature in a vacuum. The flux can then condense on the surface of the substrate material to form a thin film. The vacuum environment creates a safe zone to reduce gaseous contaminants in the deposition process to the minimum acceptable levels, allowing evaporated atoms to be transported from the source to the substrate essentially without collision. [39]

This method uses a charge holding boat or resistance coil in the form of a powder or solid bar. [49]

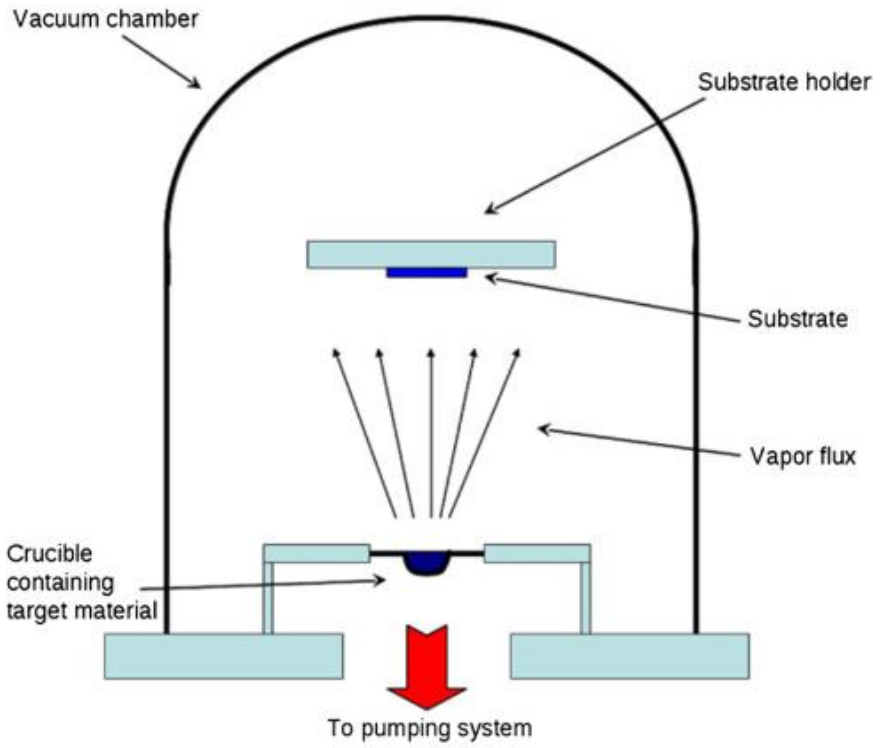

Fig.2.11. Representation of the phenomenon of thermal evaporation. [39]

2.3. Characterization techniques

Knowledge of the composition and structure of the surfaces is important. Characterization of the adhesive surface is useful for both adhesive design and failure analysis if the adhesive fails to adhere. Surface analysis is the use of microscopic chemical and physical probes that provide information about the surface area of the sample being inspected. The area of interest can be the top atomic layer or extend a few microns below the sample surface, depending on the technique used.

The analysis provides information on the chemical composition, levels of trace impurities, and the physical structure or appearance of the sampled area. Such information is important for understanding the material, testing a theory and developing better products. Many of the techniques used such as: [50]

2.3.1. Raman spectroscopy

Raman spectroscopy is a non-destructive analytical technique used to study the interaction of vibrational energies of atoms or groups of atoms within a molecule. The Raman Effect is produced by the energy exchange between the incident photon and the vibrational energy level of the molecule.

In fact, Raman microscopy is almost entirely based on the analysis of much higher intensity Stokes scattered light. The light scattered by the molecule contains a different frequency than the incident monochromatic light that corresponds to the normal vibration frequency of the molecule. When a molecule absorbs radiation, its energy increases in proportion to the photons; the increasing energy can be at the level of the molecule's electronic energy, vibrational energy, or rotational energy. This technique is complementary to infrared spectroscopy which also allows to study the vibrational modes of a material, however when compared to infrared technique, Raman spectroscopy is better. [51]

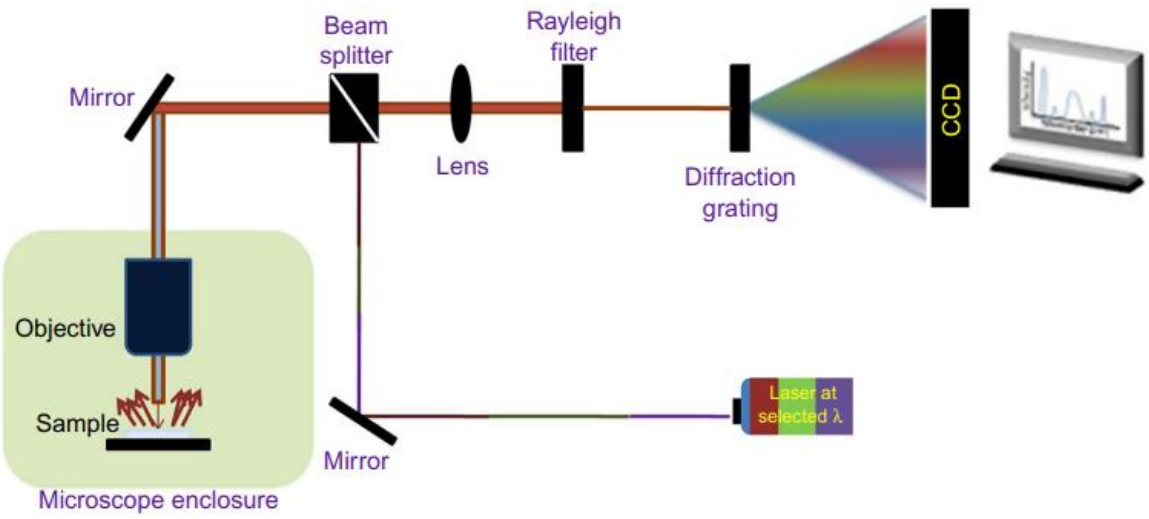

Fig.2.12. Schematic for process involved in Raman spectra. [51]

As depicted, Raman spectrometer is typically composed of light source, monochromator, sample holder, and detector. The Raman scattered light is dispersed according to wavelength and processed as Raman spectra; with a series of peaks that indicate the intensity and wavelength position of the Raman scattered light, it helps knowing many information such as photon wavelength and number, the more photons reach the detector, the

higher the intensity of light is. The spectrum is: intensity as a function of wavenumber (a value proportional to the inverse of the wavelength). [51]

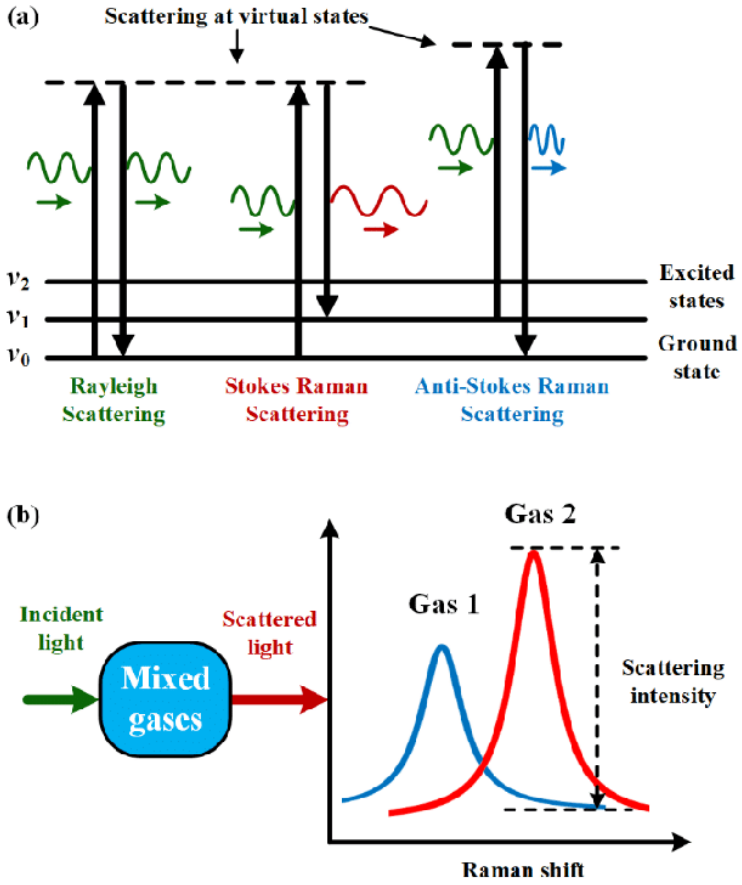

Fig.2.13. Schematic Raman spectra. [51]

2.3.2. Gas chromatography (GC)

Chromatography has a long and rich history as a separation technology. The word "chromatography" was first used by Tswett in 1906. It is derived from Greek saturation (color) and graphien (writing). Initial use of chromatography did not contain instrumental technologies such as columns and paper clomatography. [52]

As the name implies, these techniques have often been used to separate the colored components in the mixture. Today these techniques are still used with greater focus on instrumental techniques, such as gas chromatography, high performance liquid chromatography (HPLC), and supercritical fluid chromatography (SFC).

Chromatography is defined as: "A physical separation process in which the components are separated and divided into two phases, stationary and mobile phase moving in

a particular direction." And all chromatographic systems have a mobile and a stationary phase. Gas chromatography, also known as gas-liquid chromatography (GLC), is a specific type of chromatography that uses an inert gas mobile phase and a liquid stationary phase. Instrumentation is constantly improving, but the basics of gas chromatographs haven't changed and remain fairly simple.

A GC operates by introducing samples through the inlet (also called injector). Carrier gas, which is the mobile phase, passes through the inlet, and sweeps the sample onto the column, where the stationary phase is. The column is enclosed in a temperature-controlled oven. Chromatographic separation occurs as the mixture moves through the column. As the separated components of the sample leave the column, they enter the detector, which provides an electronic signal proportional to the amount of analyte to elute; and all of this steps are made to determine a presence or absence and how much a chemical compounds are present. Computer control outputs a chromatogram. The x-axis is the retention time from injecting the sample into the GC to the end of the GC run, and the y-axis is the measured response of the detector's analysis target peak. This series of peaks is more or less separate, large, or wide and by measuring the area of each peak and associating it with the total area of all peaks, the percentage of each component in the analyzed mixture is determined. [52]

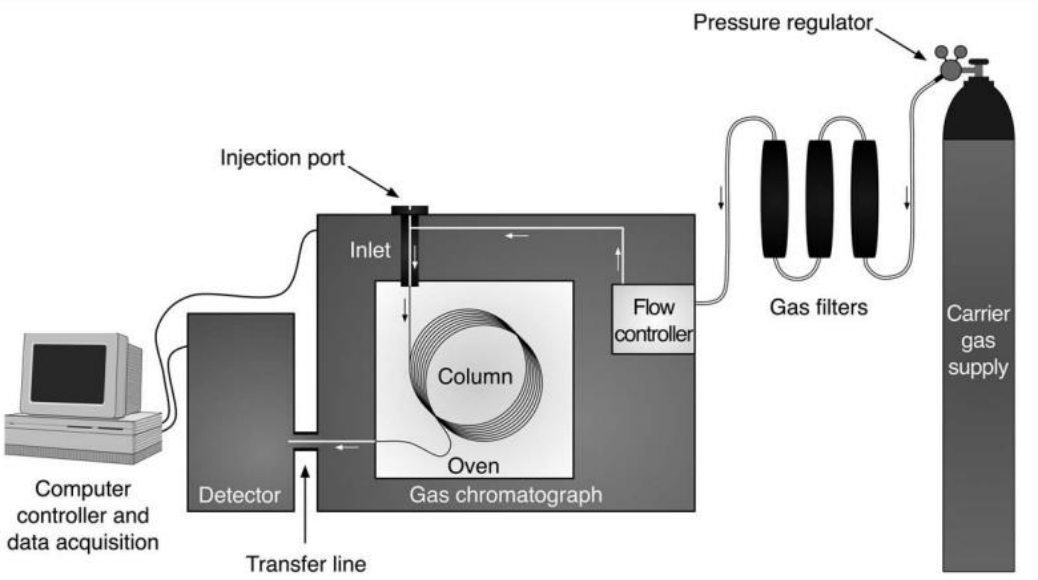

Fig.2.14. A gas chromatograph and its main components. [52]

2.3.3. X-Ray diffraction (XRD)

X-ray diffraction (XRD) is a powerful non-destructive technique for characterizing crystalline materials. It provides information on structure, phase, preferred crystal orientation (texture), and other structural parameters such as average grain size, crystallinity, strain, and crystal defects.

These X-rays are generated by a cathode ray tube, filtered to produce monochromatic radiation, collimated, focused, and directed at the sample. The interaction of the incident rays with the sample produces constructive interference (and a diffracted ray) If the condition satisfies Bragg's law:

$$n\lambda = 2d\sin\theta$$

Where: λ is the wavelength of the X-rays, n is diffraction index, d is the interplanar spacing generating the diffraction, θ is the diffraction angle.

This law relates the wavelength of electromagnetic radiation to the diffraction angle and the lattice spacing in a crystalline sample. These diffracted X-rays are then detected, processed, and counted.The sample must be in the form of a powder flattened in a cup, or in the form of a flat solid plate. X-rays are sent to this sample, and a detector analyzes a rotation of 2θ around the sample to measure the intensity of the X-rays according to the direction. For practical reasons, even the sample or the tube producing the X-rays rotates at the same time.

X-ray diffractometers consist of three basic elements: an X-ray tube, a sample holder, and an X-ray detector. [53]

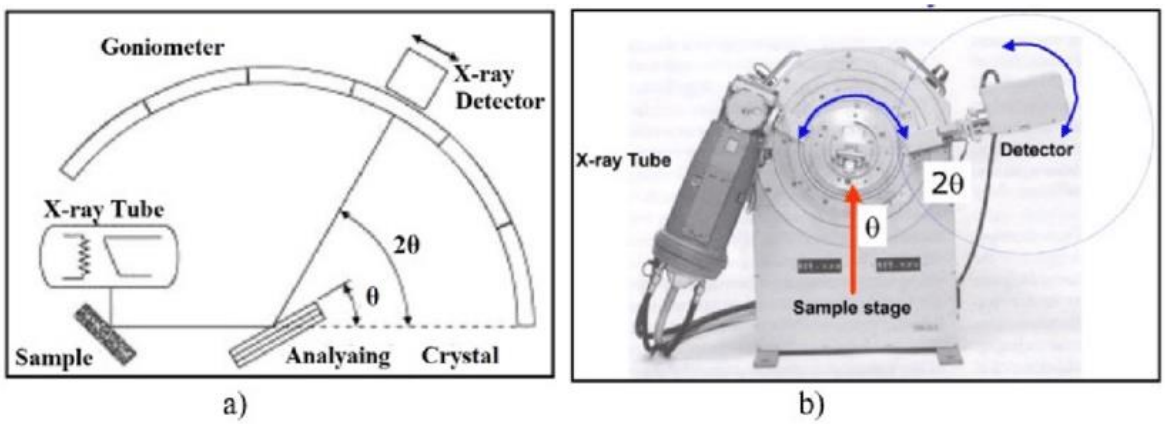

Fig.2.15. a) Schematic diagram of a XRD system; b) A Modern Automated X-RD Diffractometer. [53]

X-rays are generated from the X Ray tube (Coolidge tube) when it hits the atoms of the sample, its energy is absorbed by the electrons and re-emitted as a new X Ray that's where

the diffraction happens between atoms. The signal is recorded by the detector and graphed (intensity in function of 2θ), it helps providing information about the sample such as: the width of the peak tells about crystallite size and lattice strain and Peaks intensity tells about the position of atoms within a lattice structure. [54]

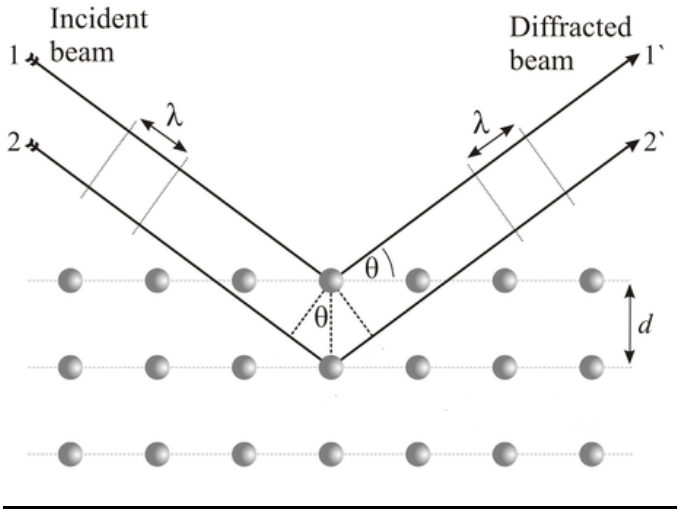

Fig.2.16. Diffraction phenomenon on atoms [54]

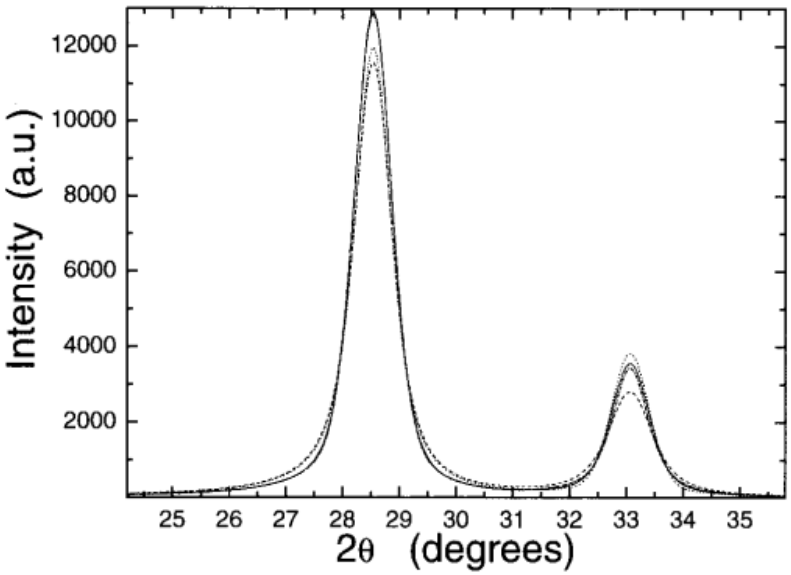

Fig.2.17. Simulated patterns for a FCC material. [54]

2.3.4. Scanning Electron Microscopy (SEM)

SEM is a convenient method for analyzing plastic surfaces. In fact, it helps any surface that survives in a vacuum. Almost all SEMs begin by sputtering the surface with a thin layer of gold metal. This makes the surface conductive if it is not yet conductive because it is a requirement; a finely focused electron beam sweeps the entire surface of the analytical sample. The beam is focused on a small probe that scans the surface of the sample. [51]

The electron beam focuses on the surface of the sample, causing ionization to a depth of a few micrometers. The energy and wavelength of the X-rays emitted during the de-excitation (the passage of an atom from one energy level to another energy level to return to its ground state) cycle are characteristic of the elements present in the top layer of the sample; although the results are not true surface analysis, but the electron microprobe allows analysis of various spots of the sample surface. [51] This technique allows us to have high resolution surface images of samples

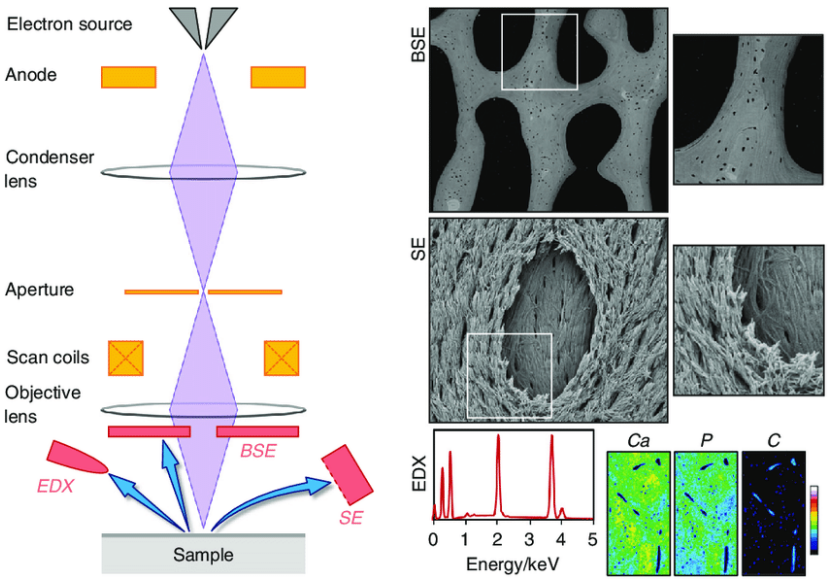

Fig.2.18. Parts of a scanning electron microscope (SEM) and the typical signals that are recorded from bone. BSE backscattered electrons, SE secondary electrons, EDX energy-dispersive X-ray spectroscopy.[51]

.

2.3.5. Atomic force Microscopy (AFM)

Atomic force microscopy (AFM) is a powerful technology that enables imaging of almost any type of surface, including polymers, ceramics, composites, glass, and biological samples. AFM is used to measure and identify various forces such as bond strength, magnetic

force, and mechanical properties. The AFM consists of a sharp tip with a diameter of approximately 10^{-20} nm attached to the cantilever. AFM tips and cantilever are micro-fabricated from Si or Si_3N_4. The tip moves according to the interaction between the tip and the surface. This movement is measured by focusing the laser beam with a photodiode. [55]

AFM operates in two basic modes: contact and tapping modes. In the contact mode, the AFM tip is in continuous contact with the surface. In contact mode, the AFM tip is always in contact with the surface. In contrast, in tapping mode, the AFM cantilever vibrates on the surface of the sample, causing the tip to only make intermittent contact with the surface. This process helps reduce the shear forces associated with tip movement. Tapping mode is the recommended mode commonly used for AFM imaging. Contact mode is only used for certain applications such as Force curve measurement. Unlike electron microscopy, which provides a 2D projection or image of a sample, AFM provides a true 3D surface profile. [55]

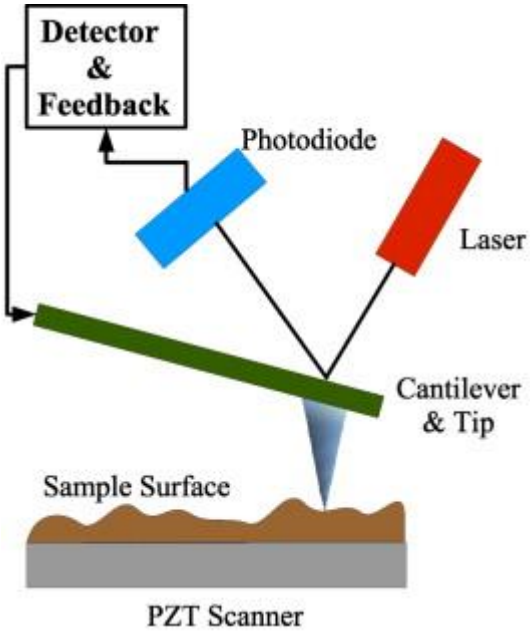

Fig.2.19. Atomic Force Microscope. [55]

2.3.6. Fourier transforms infrared spectroscopy (FTIR)

The Fourier Transform Infrared Spectrometer (FTIR) is one of the instruments based on infrared spectroscopy. This is the most modern type and is preferred over other distributed spectrometers due to its high accuracy, speed, improved sensitivity, easy operation, and non-destructive process.

The basis of infrared spectroscopy is the atomic vibration of molecules that absorb only certain frequencies and energies of infrared light. Different molecules have different infrared spectra, so molecules can be detected and classified by FTIR.

The FTIR spectrometer essentially uses an interferometer to measure the energy transferred to the sample. The infrared rays emitted from the blackbody reach the interferometer, where the spectral coding of the signal takes place. The resulting interferogram signal is transmitted or reflected through the surface of the sample where energy of a particular wavelength is absorbed. The beam eventually passes through the detector and is further transferred to the processing computer for the Fourier transform of the energy signal. [56]

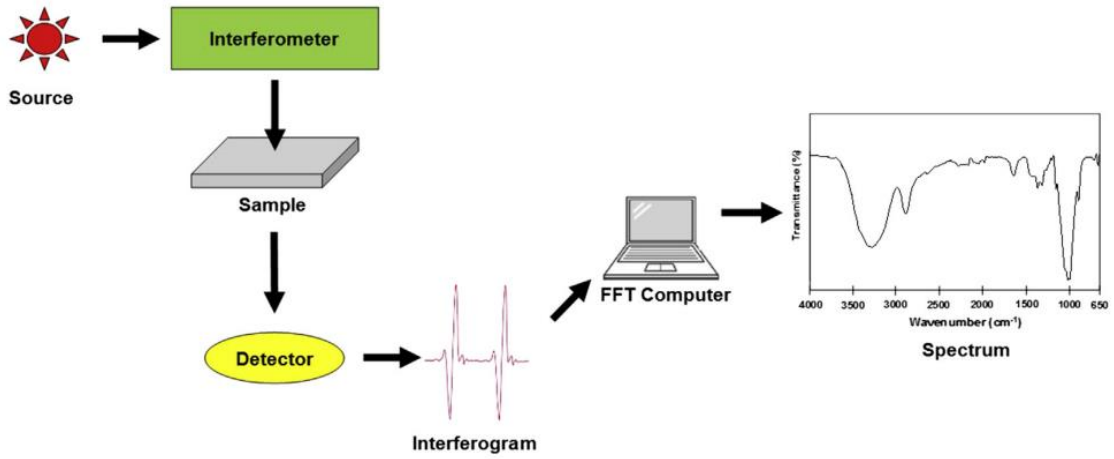

Fig.2.20. FTIR processing. [56]

This technique helps identify chemical bonds in a molecule by producing an infrared absorption spectrum in function of wavenumber. Where the IR spectrum is divided into three wavenumber regions: far-IR spectrum (<400 cm^{-1}), mid-IR spectrum (400-4000 cm^{-1}), and near-IR spectrum (4000-13000 cm^{-1}). The mid-IR spectrum is the most widely used in the sample analysis, but far- and near-IR spectrum also contributes in providing information about the samples analyzed.

The mid-IR spectrum is divided into four regions: (i) the single bond region (2500-4000 cm^{-1}), (ii) the triple bond region (2000-2500 cm^{-1}), (iii) the double bond region (1500-2000 cm^{-1}), and (iv) the fingerprint region (600-1500 cm^{-1}). [57]

2.3.7. Ultraviolet–visible–Infrared spectrophotometer:

Ultraviolet-visible spectroscopy deals with the interaction between matter and electromagnetic radiation in the UV-visible range. The ultraviolet (UV) range roughly covers the 10-380 nm region of the electromagnetic spectrum. It is usually divided into three main sub-regions: UVA in the range 320-380 nm. UVB in the range of 280-320 nm; In addition, the range of 10-200 nm, which is only investigated by vacuum measurements, is also called vacuum ultraviolet (VUV). The visible (Vis) range covers the spectral range from 380 to 750 nm.

UV-Vis spectroscopy refers to the excitation of the surface electrons of an atom involved in the formation of a molecule, and is often referred to as "electron spectroscopy". Measurements in the UV-Vis range are usually performed in transmission, reflection, and photoluminescence modes. Transmittance and reflectance measurements should be recorded and compared with reference material, but photoluminescence detection can be considered an absolute measurement. [58]

The physical principles underlying this method are not complicated, making the measurement simple and robust. Light of known wavelength and intensity is directed at the sample and the final intensity after passage is measured by the detector. By comparing incident radiation (I_0) and transmitted radiation (I), you can easily calculate the amount of light absorbed by the sample at that particular wavelength. Using the Beer–Lambert law, this absorbance can be used to measure the concentration of known solutes.

$$A = log_{10}\left(\frac{I_0}{I}\right) = \varepsilon . C . L$$

Where, A is absorbance, ε is the molar absorbtivity ($L\ mol^{-1}\ cm^{-1}$), c is the concentration of the dissolved solute ($mol\ L^{-1}$), and L is the path length (cm). [59]

UV-vis spectroscopic data can give the measurement of wavelength and intensity of ultraviolet and visible light absorbed by the sample as a function of wavelength.

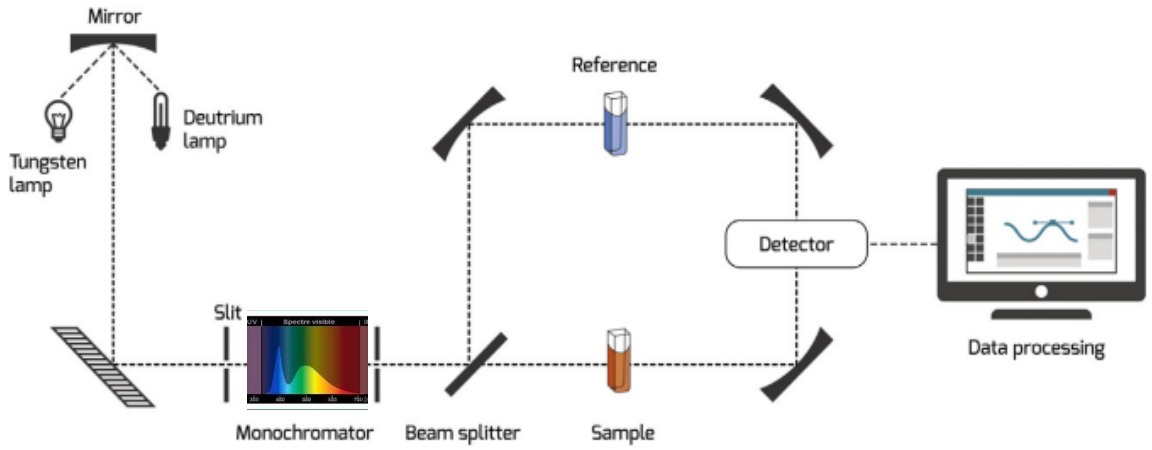

Fig.2.21. Schematic representation of UV-Vis-IR spectroscopy. [59]

.

2.3.8. Photoluminescence Spectroscopy (PL)

Photoluminescence is the process by which a substance absorbs photons and then emits them again. PL spectroscopy analyzes the distribution of energies involved in the light absorption and photoelectron emission processes, photoelectron emission efficiency, and their temporal characteristics. Due to its non-destructive and non-contact properties, photoluminescence spectroscopy is suitable for solids, solutions, solid suspensions, and gaseous materials, making it extremely versatile and sensitive for molecular detection and structural analysis. [60]

Luminescence, the emission of visible light, occurs when an energy source (laser, UV lamp, etc.) knocks an electron out of its stable "ground" state and elevates it to an "excited" state. When an electron returns to its normal ground state, it emits energy, much of it in the form of visible light. In almost all cases, the emitted light has less energy in the electromagnetic spectrum than the original light from the energy source. Wavelength and energy are inversely proportional, so the lower the energy, the longer the wavelength is. Therefore, the PL spectrum always contains a wavelength range higher than the wavelength of the excitation source. It comes with two forms, FLUORESCENCE "it lasts less than 10 nanoseconds and emission of visible light occurs while a UV source is turned on" and PHOSPHORESCENCE "it lasts more than 10 nanoseconds and the emission of visible light occur after a UV source is turned off". [61]

It measures the PL intensity in function of wavelength to provide information about purity and crystalline quality, and identify certain impurities in materials for energy devices.

2.3.9. Thermoluminescence Spectroscopy (TL)

Thermally stimulated luminescence (TSL) is the light produced by heating a solid. Light is observed only after the solid is irradiated, and heat acts only as a trigger. The main use of TSL is for radiation dose measurement. This is because for some materials it has been shown that the emitted light is proportional to the absorbed dose to which the material is exposed. However, in the 1950s, it was recognized that TSL could be used not only for dosimetry and dating, but also for other purposes such as measuring the efficiency of surface catalysts and measuring impurities in rocks. Thermoluminescence is also very sensitive to defects in the material under investigation and can also be used to investigate these defects. [62]

The presence of defects and their position with respect to the conduction and valence bands strongly influences the emission properties of the material. Thermoluminescent spectra, also known as glow curves, can be used for defect analysis, trap depth determination, radiation dose determination, and more. [60-63]

The glow curve is a plot of luminescence intensity as a function of temperature, smooth, continuously distributed over wider temperature intervals, and resulting in a wider glow peak. Each peak corresponds to a different trap depth and is obtained by the release of electrons from these traps of different depths. Thermoluminescent diagrams show that TL intensity increases with increasing temperature and reaches maximum first; this may be due to increase in probability of evacuation of traps, which in turn increases the probability of radiative recombination of electrons and trapped holes, the decrease in intensity with temperature may be due to de-trap, which eventually decreases when the number of carriers is exhausted. The different peaks in the spectrum correspond to different electron traps at different depths. [64-67]

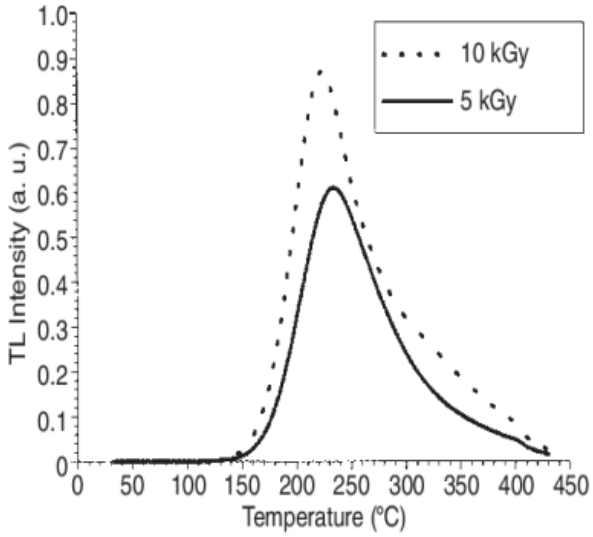

Fig.2.22. Thermoluminescence intensity as the function of temperature. . [60-63]

2.3.10. X-Ray Fluorescence Spectroscopy (XRF)

X-ray fluorescence (XRF) is an established method of material analysis suitable for use in the inline semiconductor industry. The sample to be analyzed is irradiated with X-rays or gamma rays, and electrons in the nuclear plane are excited to the excited state. Radiation attenuation of these electrons from the excited state back to their respective ground states leads to fluorescence or emission of "secondary" X-rays. This is a characteristic of the energy level of each atomic species and is therefore an element present in the sample. The spot size of product wafers can be reduced to 100 nm or less.

The XRF signal strength of each atomic type correlates directly with the number of atoms present, so the XRF signal can be used as a direct measure of the thickness of a metal or alloy. The main strength of XRF as a metrology is that it can evaluate thin film thickness and alloy concentration regardless of numerical modeling methods. The high frequency transmission of metal makes it possible to measure samples as thick as a few microns. In contrast, XRF can theoretically be used to measure any thin layer less than 10 nm thick. The biggest challenge when measuring very thin slices is the long acquisition time required for the XRF detector. [68]

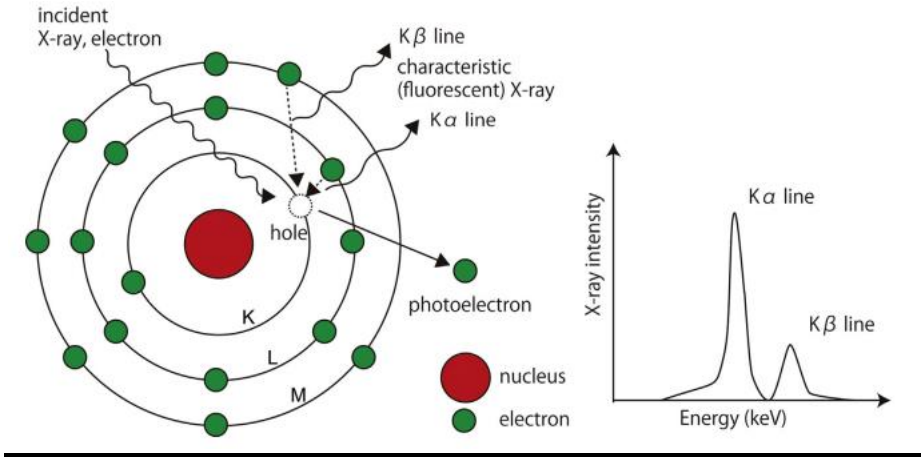

Fig.2.23. Thermoluminescence intensity as the function of temperature.[69]

The mechanism of characteristic X-ray generation is shown in the figure above. The impact of high-energy electrons and high-energy X-rays hits the bound electrons of the target atom. After the electrons are emitted, the outer shell electrons fall into the free inner shell and emit characteristic X-rays with an energy equal to the energy difference between the outer and inner shell energy levels. Characteristic X-rays produced by high-energy X-ray radiation are called "fluorescent X-rays." Each element contained in the sample produces a characteristic set of X-ray fluorescence (“fingerprints”) that is unique to that particular element, that is why XRF spectroscopy is an excellent method for qualitative and quantitative analysis of material composition. [69]

Chapter 3:

3.1. Introduction :

The first part of this chapter deals with the elaboration method used for the deposition of thin films based on FeS_2. While the second part deals with the characterization techniques used to determine the different properties of these thin-films, the interpretation of the obtained results will discussed in details.

3.2. Substrate Preparation:

The substrate is previously prepared based on $Si_2Al_2O_5$-$(OH)_4$ phyllosilicates by going through several steps: first it is in its raw rock form, then it is ground into powder to react with some chemicals (acid) to obtain a paste that can be shaped as desired. Once it is done, it calcined in a furnace at 700 °C to have the final product ready to be used for the deposition of thin-films.

For the implantation of FeS_2 nanocrystals, the physical PVD method was chosen, specifically thermal evaporation cited in Chapter 2, because it is the available technique but must go through the process of sulfidation (the reaction allowing the introduction of a sulfide ion into a molecule or material; this process is widely used to convert oxides to sulfides, but also has to do with corrosion management and surface modification).

3.3 Characterizations techniques:

3.3.1. X-ray Diffraction (XRD) :

XRD characterization was performed using a RIGAKU ULTIMA IV type θ [2θ]° diffractometer, where X-rays are produced by a copper K_α emission source. X-ray Diffraction (XRD) is a technique for the characterization of crystallized materials, whether they are solid or powder; it is mainly applied to inorganic materials: minerals, metals, and alloys. The material and structure were determined by comparing the spectra obtained with the database called ASTM (American Society of Testing Materials) using High-Score Plus analysis method.

Fig.3.1 collects all the X-ray diffraction spectra of the nanocrystals implanted on a phyllosilicates-based substrate $Al_2Si_2O_5(OH)_4$. We have three samples as shown in the figure. The first sample is described as the substrate, the second one corresponds to the formation of FeS_2 nanocrystals using the B_1 magnetic field, and the third one corresponds to the sample using the B_2 magnetic field. The XRD measurements for the substrate show that the resulted

material is essentially made up of minerals associated with silica and alumina. The XRD spectrum corresponding to the substrate based on phyllosilicates materiel indicates the presence of quartz in non-negligible quantity and the calcium sulfate needed for CO_2 sequestration.

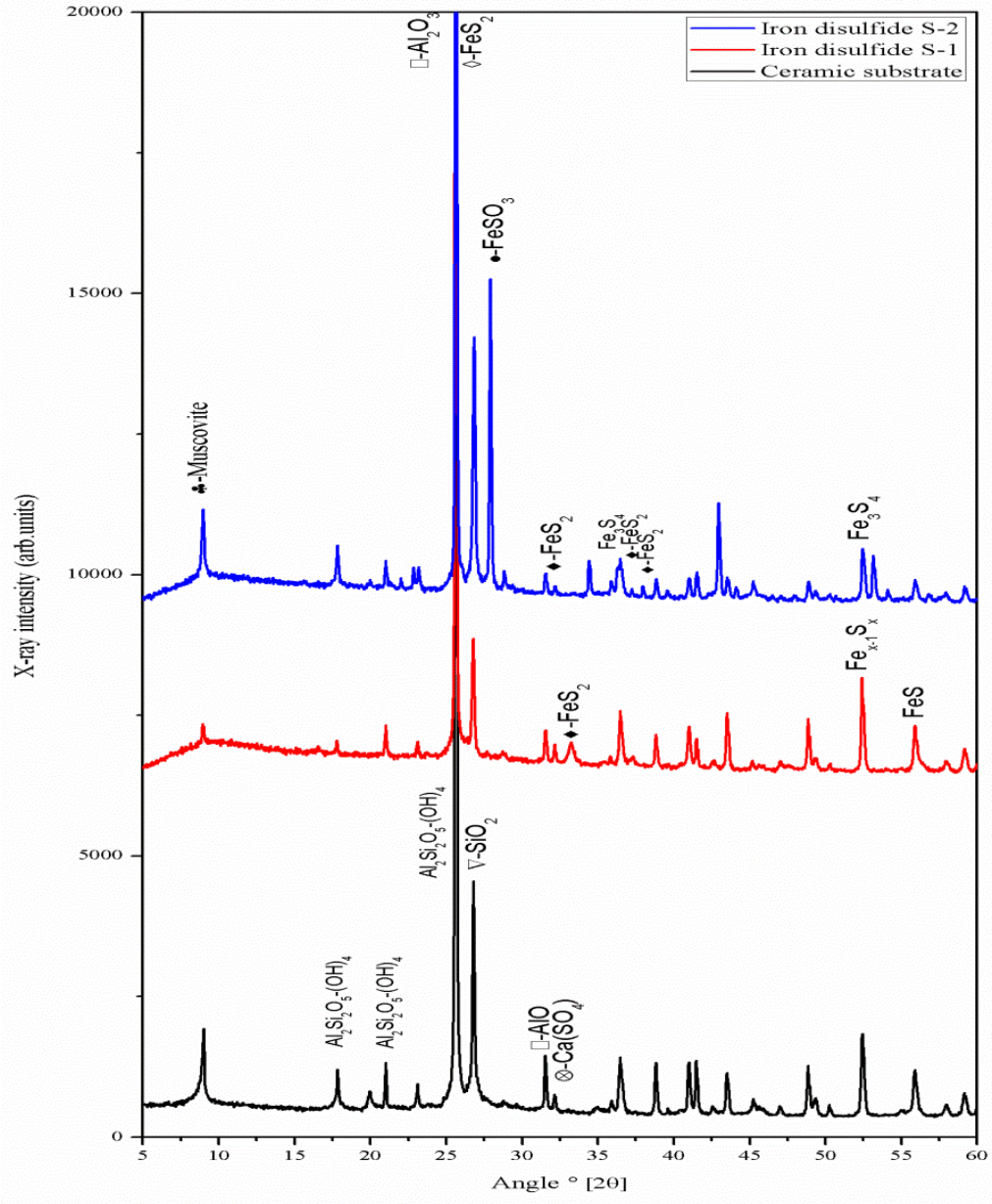

Fig.3.1. X-ray diffraction patterns for the three samples, black line: substrate, red line: formation of FeS_2 using B_1 and blue line: formation of FeS_2 using B_2

Indeed, the peaks at 17 (2θ), 21 (2θ) and 26 (2θ) are the most intense peaks and are well characteristic of an $Al_2Si_2O_5(OH)_4$ especially of 26 (2θ). So, sharp-prominent peaks correspond to γ transformed to α-Al_2O_3 alumina and was compared with the Al_2O_3 data reported in datasheet with Reference code: (01-076-0144) and the other peaks correspond to SiO_2 compared with (ASTM datasheet Reference code: 01-083-2465) which almost mushed. In the second and third XRD spectrum noted S-1 and S-2 in red and blue lines, samples were sulfided at 550°C for one hour and we notice a formation of new peaks which have no relation with the previous one and which seem to be related to iron disulfide.

The mineralogical and chemical compositions of the substrate was previously investigated with XRD, it indicated after calcinations at 600 C° that quartz been together with phyllosilicate is the main minerals of the substrate. The presence of quartz results in increasing the SiO_2 content. Therefore, the substrate falls in the category of high-silica. [70] It was also observed, that powder consisted also of a small amount of illite phase. [71]

On the other hand FeS_2 was previously investigated with X-Ray diffractometry, it revealed the presence of triolite (FeS), marcasite along with pure pyrite at high concentration of iron ions [72], the mixture of Fe-S compounds is probably due to pyrite decomposition and at 450C° sulfuration temperature the cubic phases are formed. [73] Using the standard card JCPDS 71-0053 in the process of hydrothermal carbonization, no influence on the crystal structure was found since the lattice constant calculated a = 5.418 Å, is in good agreement with the value in the reference. [74]

3.3.2. Scanning Electron Microscopy (SEM) Micrographs:

Scanning electron microscopy (SEM) is a characterization technique that gives us high resolution surface images of samples. Morphology of the Two samples were investigated using it, the 1st two images belongs to sample 1 where nanocrystals where formed using B_1 magnetic field; showing us pile of hexagonal plates due to the presence of T=Troilite (FeS) and the lack of cubic phases; there is irregular and variable sizes h_1=0.8 µm, a_1=1.6 µm, h_2=0.84µm, a_2=2.9µm. The shape variation from irregular thin nanoplates morphology to regular thick hexagonal nanoplates is strongly dependent on the reaction temperature, different crystal directions and aging time; this can be distinguished in two ways, one direct growth path from small to large size at high temperature. Yet, the other one is all about aging time with low temperature. The Ostwald growth mechanism is also suggested to be the reason of the variation shapes; it consists of a competitive growth, large nanoplates get more in the

size using seeds that combined randomly at the beginning to form smaller irregular nanoplates.

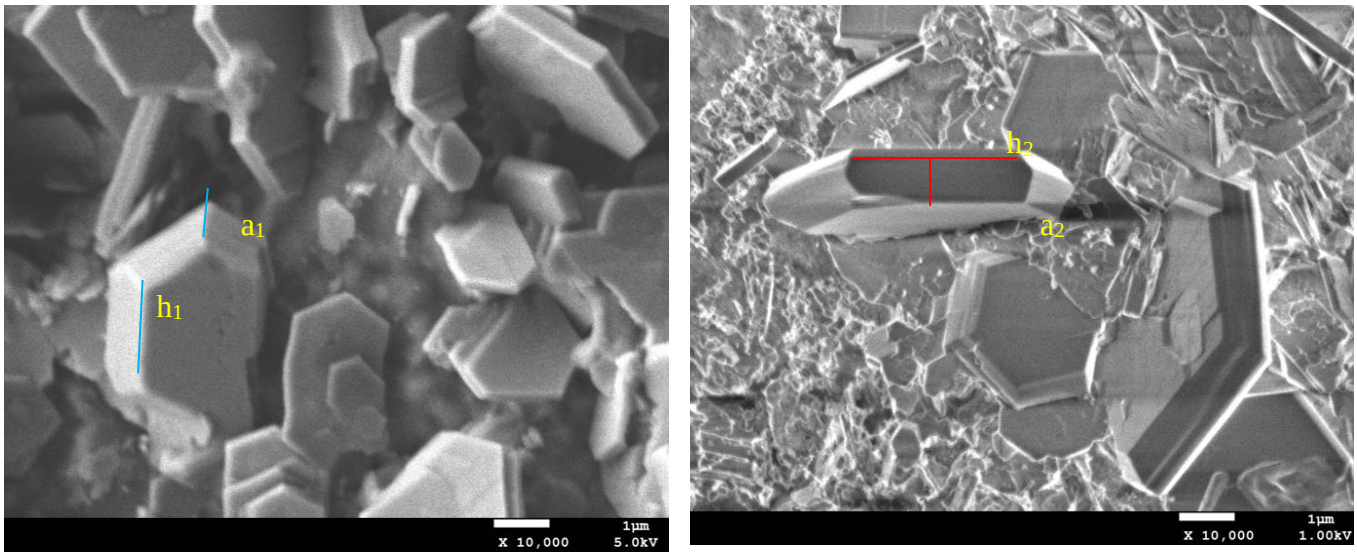

Fig.3.2.SEM images for sample 1 (formation of FeS_2 using B_1)

Fig.3.2 represents Sample 2 where nanocrystals where formed using B_2 magnetic field; the XRD showed us that S-2 is rich with cubic phases, pyrite (FeS_2) and greigite (Fe_3S_4), that is why it can be distinguished that there is a presence of cubic shapes and nanotubes with dissimilar diameter and length with an accumulation of nano grain.

Both samples haven't the same morphology; the difference is caused by the magnetic field applied, since the material is ferromagnetic it will definitely react with B_1 and B_2 no matter it location. This helps accelerate the deposition of the thin layer and its intensity control the morphology by triggering the atoms into following the same direction as the field and that is how morphology changes by changing the intensity.

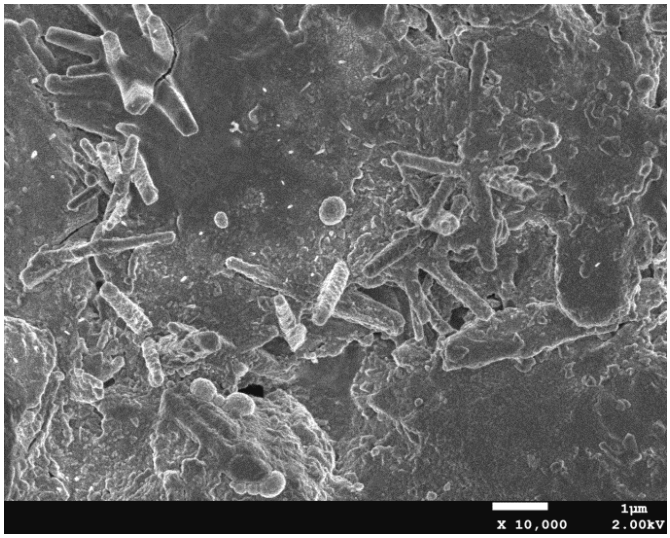

Fig.3.3.SEM images for sample 2 (formation of FeS_2 using B_2)

In other studies, pyrite FeS_2 nanotube have been fabricated using layer by layer assembly on ZnO nanorod arrays in combination with sulfurization at 350 ◦C for 2 h with a diameter D=120–140 nm, wang et al. [75] figured out that it has high corrosion resistance, enhanced photoresponse, rapid electron transport performances and electrochemical stability compared with FeS_2 nanoparticle structure which make it perfect for photovoltaic and catalysis applications. [75] And the pyrite nanotubes synthesized are several microns in length.

The hexagonal plate pyrites also was synthesized with other processes, the quadrangular plates and other irregular forms with a size of 1–20 μm without defects are observed as the products of the hydrothermal method; and the thick flake and granular pyrites appear in the products of the solvothermal method. [76]

3.3.3. Optical properties

a) Spectrophotometry UV-Vis-IR

Spectrophotometer UV-Vis-IR uses ultra violet [100-400nm], visible [400-800nm] and an infrared [800-10^4nm] regions, the interaction with light measures the reflectance which helps determining the absorbance using the Kubelka-Munk transformation. In fig.3.4 below, the reflectance spectra of three samples (1, 2 and substrate) respectively, are represented in range of wavelengths [350-2450nm], clearly there is a difference between the three curves probably caused by the magnetic field applied.

It can be observed that the diffusive reflectance exhibits minimum value in the UV region around 350nm for the three samples (7%, 15% and 25%); it increases in the visible region to reach (70%, 72% and 85%). However in the IR domain each sample reaches it maximum diffusive reflectance, at 2275nm substrate, S_1 extend to 110% and 95% respectively; but S_2 get to 91% at 2100nm. The maximum of reflectance determine the low (minimum) absorbance where possibly the band gap area is.

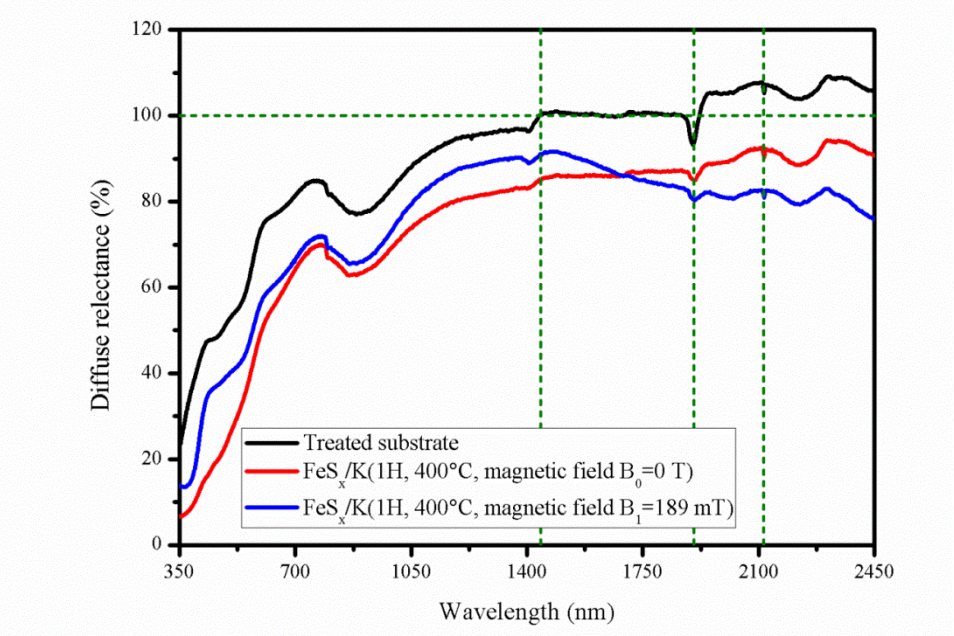

Fig.3.4. Reflectance spectra for three sample, susbtrate and two samples with the formation of FeS_2 using B_0 and B_1

FeS_2, is a semiconductor with high iron content, is expected to be a strong UV absorber. The contribution of photons in semiconductors materials helps pass the electrons from the valence band to the conduction band. This process creates the so-called electron-hole pairs that can easily react with adsorbed molecules on the surface of the semiconductor and trigger redox reactions. The study of clean pyrite and exposed pyrite to air, demonstrated that pyrite has UV-photocatalytic activity, and even catalytic activity (in the absence of UV) provided that oxides species are present on the surface. [77]

In a previous UV-Vis spectra absorption, FeS_2 nanocrystals E_g = 1.94 eV and FeS_2 was reported as a narrow band gap semiconductor (0.95-1.2eV) showing absorbance across the entire visible region. [78]

Band gap can be calculated using tauc plot but after getting the absorbance plot, the tauc equation is:

$$(\alpha hv)^n = \alpha_0(hv - E_g) \qquad 3.1$$

With α,α_0, hv, E_g are respectively, absorbance, constant, Planck max and gap energy

$$\alpha = \log\left(\frac{I_0}{I}\right) \qquad 3.2$$

Where I_0 is incident light and I is transmitted light.

And hv can be determined using $hv = E = \frac{hc}{\lambda} = \frac{1240\ (eV.nm)}{\lambda\ (nm)}$ 3.3

While n = ½ for indirect band gap. [81]

The band gap energy calculated for sample 1 = 1.11eV and for sample 2 = 1.12eV the slight difference likely caused by the variation in nanoparticles size and the different magnetic field used for both samples.

b) Photoluminescence

The absorption and emission spectra of the three samples Fe/Substrate, FeS_2/Substrate (B_0) and FeS_2/Substrate (B_1) are given in the PL fig below in the wavelength range from 350nm to 650nm. All samples are triggered at 350nm; there is a variation of peaks large and sharp at different wavelengths. The curves are almost regular at [375-450nm] and then it increases to reach the intense peak at 525nm for FeS_2/Substrate (B_1) and 515nm for FeS_2/Substrate (B_0) after that it decreases gradually.

Using the photoluminescence intensity and wavelengths, the width of the band gap can be determined

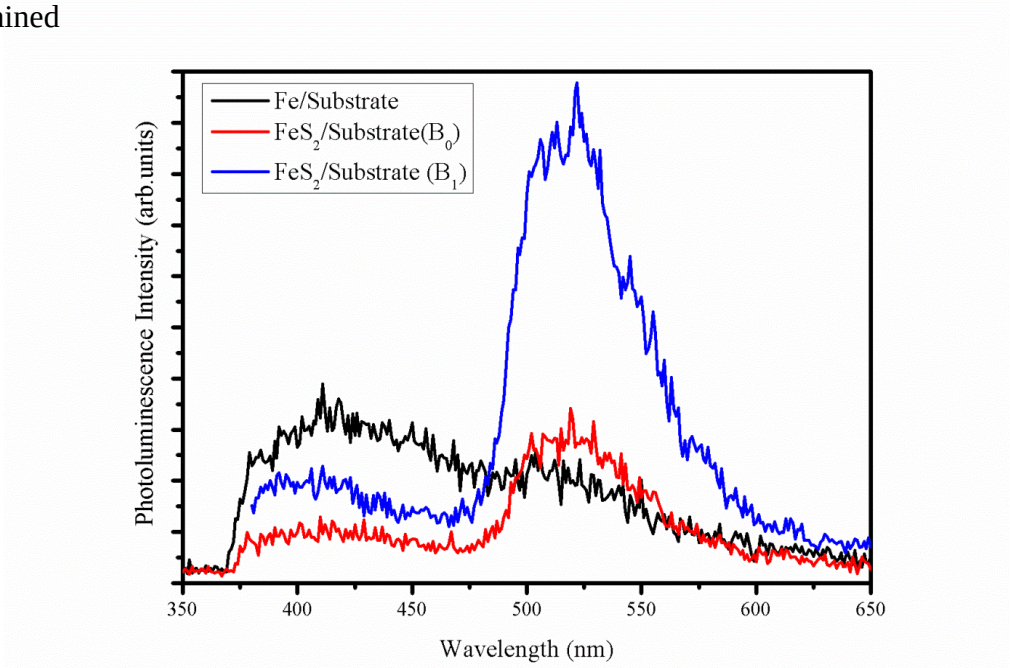

Fig.3.5 Photoluminescence spectra for three sample, susbtrate and two samples with the formation of FeS_2 using B_0 and B_1

It was mentioned in [79] that high peak at 437nm to E_g = 2.84 eV for nanocrystals (NCs) characterized at room temperature is caused by FeS presence oxygen contamination; this results were confirmed using the Raman data. And NCs synthesized with oleylamine organic compound $C_{18}H_{35}NH_2$ showed a sharp, narrow centered at 726nm with E_g = 1.71eV compaired to natural pyrite E_g = 1.51 eV at 816nm. The discrepancy of 0.20 eV is attributed to the nanosize particles. [30]

3.3.4. Gas treatment:

Gas treatment helps us study the behavior of FeS_2 under variable concentrations of gas; we used for this experiment CO_x and NO_x at four different concentrations C_1, C_2, C_3 and C_4, 50sccm, 100sccm, 150sccm, 200sccm, respectively. Three samples were placed in the vacuum chamber where each one is submitted to tension using different range and step. So, the first and third one are defined as FeS_2 nanocrystals implanted into ceramic substrate in presence of magnetic fields B_0, B_1, respectively, and the interdigitated Al electrodes. The second one is under B_2 magnetic field without interdigitated Al electrodes. The purpose of this process is to identify which one of the samples is most sensitive at a specified concentration; in order to do that we determine the sensitivity by:

$$S = \left| \frac{R_0 - R}{R_0} \right| \text{ and } R = \frac{V}{I} \qquad 3.4$$

Where V, I, R are tension, current and resistance, respectively.

a) I(V) measure with CO_x

The graph represents current vs tension for sample 1 and 3, at tension domain [0-2] volt. We can observe that it is almost a line graph, current increases until its max for the four concentrations, which means that tension and current are proportional. Indeed, the sample N° 2 is without interdigitated electrodes to compare with the other samples, as for the gases used, NO_x is more toxic than CO_2 and we want to detect it without additional supports as we did with the other samples (The Al circuit deposit on the back side, see Fig.3.7).

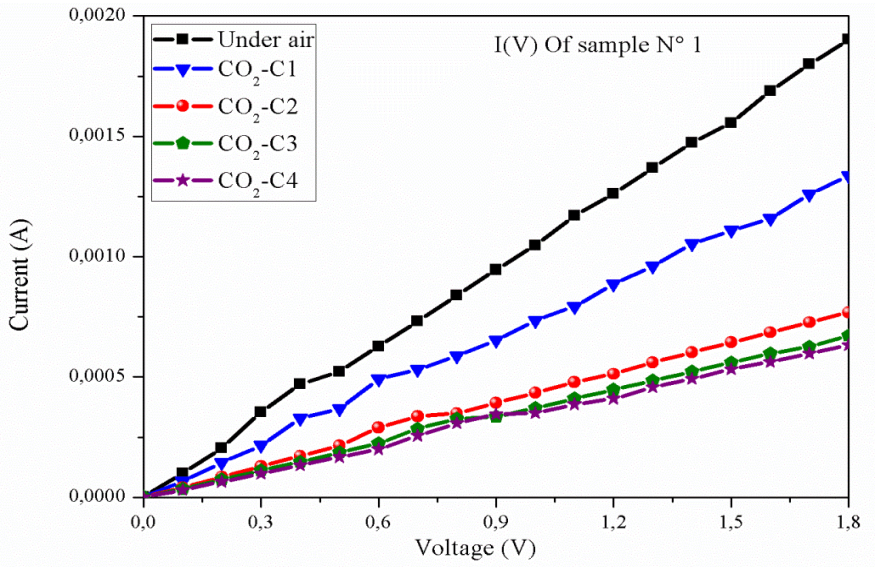

Fig.3.6 current in function of tension for sample 1, formation of FeS_2 using B_0

I-V measurements provide information on the contact type, particle-to-particle, and electrode-particle contact formation. The CO_2 sensing ability of FeS_2 nanostructured films annealed at 400 °C was tested in a homemade gas chamber. The characteristic I-V curves of the two samples (1 and 3) in an air and CO_2 environment of [0-200] sccm concentration were measured for 5 minutes at room temperature and plotted in Figure 3.6. This figure clearly shows a linear ohmic behavior for both films. When the environment was changed from CO_2 to air, the current tracking rate at the same voltage is increased by a factor of ten in current. This can be attributed to the oxidizing nature of the CO_2 gas, which leads to the increase in resistance of the n-type material. However, the gas nature of air leads to the decrease in Ohmic resistance.

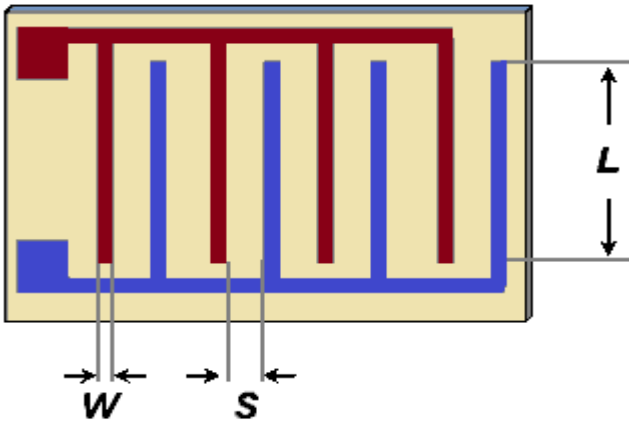

Fig.3.7 Interdigitated electrodes deposited in back side of the sample

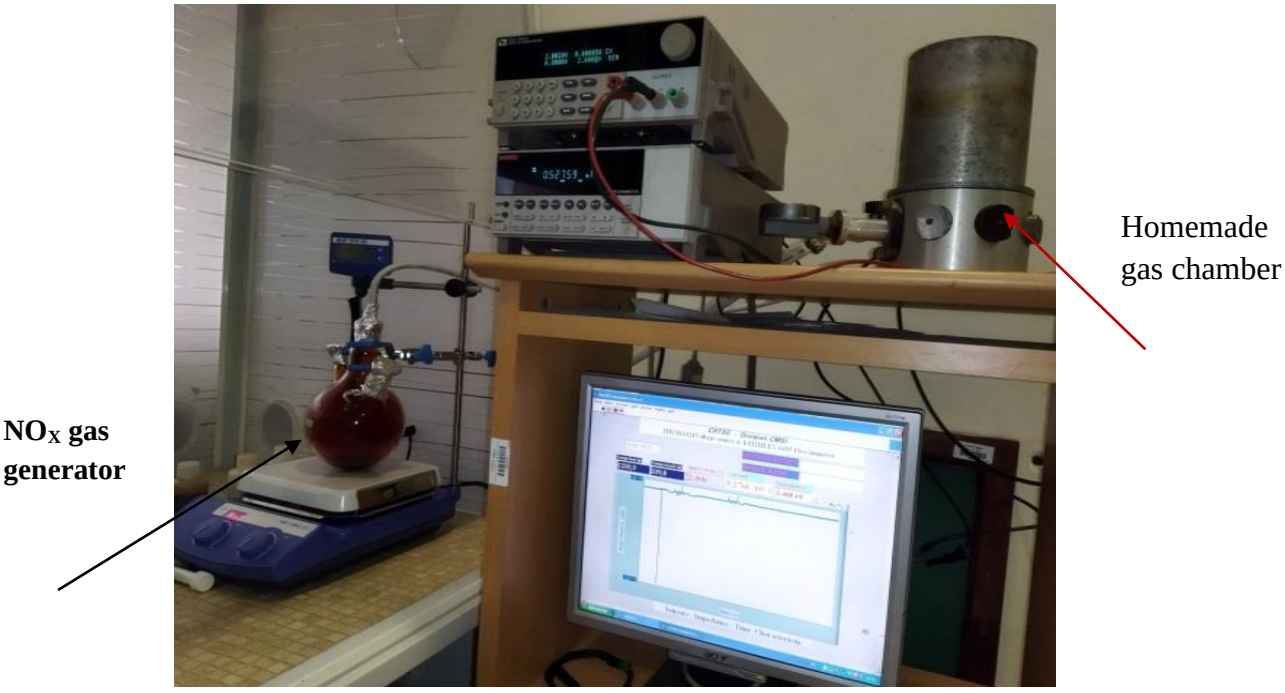

Fig.3.8 Experimental montage for homemade gas chamber

Table 3.1 calculation of resistance and sensitivity for sample 1

V = 1.2 v				
I_0 (A)	I_1 (A)	I_2 (A)	I_3 (A)	I_4 (A)
$1.25x10^{-3}$	$0.87\ x10^{-3}$	$0.5\ x10^{-3}$	$0.37\ x10^{-3}$	$0.25\ x10^{-3}$
R_0 (Ω)	R_1 (Ω)	R_2 (Ω)	R_3 (Ω)	R_4 (Ω)
$0.96\ x10^{3}$	$1.38\ x10^{3}$	$2.5\ x10^{3}$	$3.24\ x10^{3}$	$4.8\ x10^{3}$
S_0	S_1	S_2	S_3	S_4
0	0.42	1.6	2.38	4

As shown in Fig.3.7, the interdigitated circuit greatly assists in the collection of charge carriers, resulting in an I(V) characteristic in the presence of CO_2 gas. The response of the sample is therefore studied in the case where there is no gas injection (Under air) as shown in Fig.3.6. The same operation is performed with sample No. 3, but here the only difference is related to the magnetic field intensity used during the process of elaboration of FeS_2 nanocrystals. Table 3.1 shows the resistance values, which increase proportionally, revealing an Ohmic character.

Sample.3:

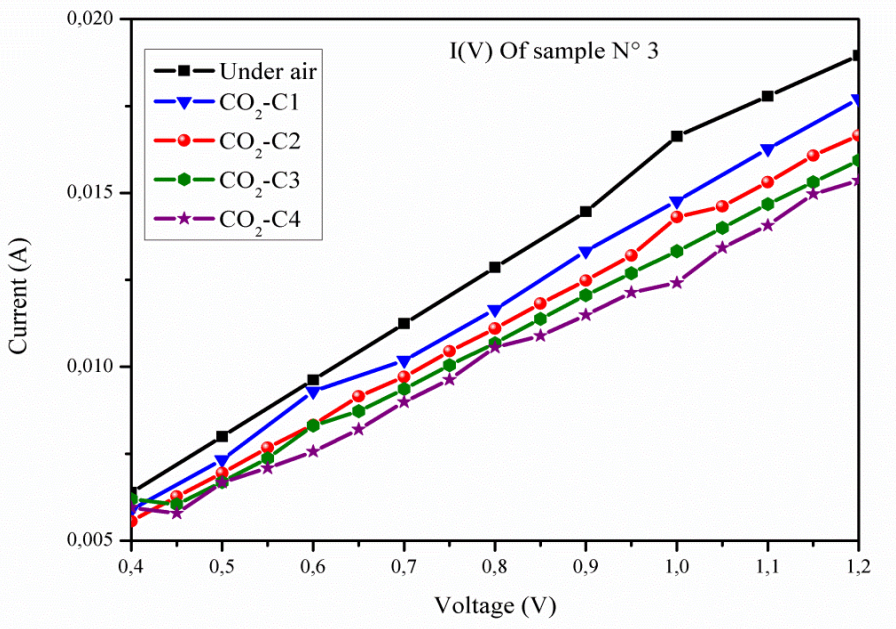

Fig.3.9 current in function of tension for sample 3, formation of FeS_2 using B_1

Table 3.2 Calculation of resistance and sensitivity for sample 3

V = 0.9 v				
I_0 (A)	I_1 (A)	I_2 (A)	I_3 (A)	I_4 (A)
13.75×10^{-3}	12.81×10^{-3}	12.5×10^{-3}	11.87×10^{-3}	11.25×10^{-3}
R_0 (Ω)	R_1 (Ω)	R_2 (Ω)	R_3 (Ω)	R_4 (Ω)
0.065×10^3	0.070×10^3	0.072×10^3	0.075×10^3	0.08×10^3
S_0	S_1	S_2	S_3	S_4
0	0.07	0.10	0.15	0.23

b) I(V) Measure with NO_x

For sample 2 NOx was used as a gas and it gave us the perfect line graph for the four different concentrations in a tension domain [0.3:0.1:0.7], the proportionality of current and tension is obvious.

Table 3.3 Calculation of resistance and sensitivity for sample 2

V = 0.6 v				
I_0 (A)	I_1 (A)	I_2 (A)	I_3 (A)	I_4 (A)
1.1×10^{-5}	0.72×10^{-5}	0.7×10^{-5}	0.69×10^{-5}	0.67×10^{-5}
R_0 (Ω)	R_1 (Ω)	R_2 (Ω)	R_3 (Ω)	R_4 (Ω)
0.54×10^5	0.83×10^5	0.86×10^5	0.87×10^5	0.9×10^5
S_0	S_1	S_2	S_3	S_4
0	0.53	0.59	0.61	0.66

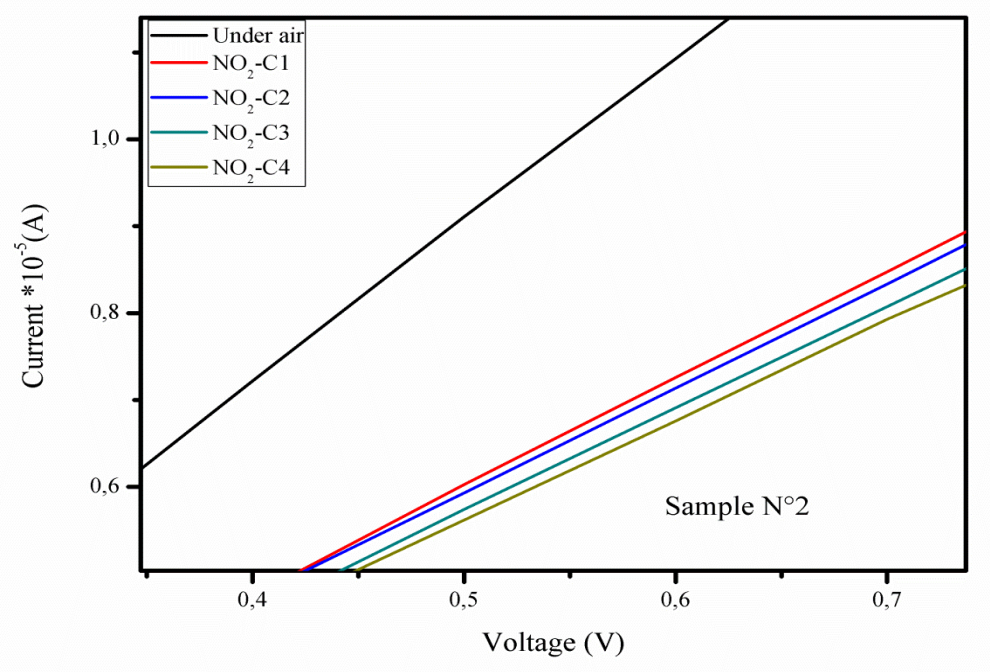

Fig.3.10 current in function of tension for sample 2,
formation of FeS_2 using B_2

Gas interacts with the surface of the material that means the surface area, porosity and properties of the material contribute overall gas sensitivity; and it depends on the resistance and the resistance variation is is explained by a loss or gain of electron.

Conclusion

In this work, iron disulfide nanocrystals were elaborated by several steps starting with the physical deposition of iron in vapor phase on a phyllosilicate substrate $Si_2Al_2O_5$-$(OH)_4$. Then, a sulfidation annealing process was performed to enrich and saturate the Fe-S chemical bonds leading to the elimination of the oxide bond formation. The sulfurization process is carried out in a suitable quartz tube equipped with nitrogen gas inlets and outlets for the control of the sulfur vapor preventing, for this purpose, the formation of toxic gases namely H_2S and SO_x (x=1.2.3).

Our samples were analyzed by XRD (CRTI). Indeed, the obtained spectra reveal, for a substrate, peaks well characteristic of an aluminosilicate $Al_2Si_2O_5(OH)_4$, in particular a peak with strong predominance corresponding to the γ-alumina transformed into α-Al_2O_3, and were compared to the data of Al_2O_3 reported in the data sheet with the reference code: (01-076-0144). For the XRD spectra noted S-1 and S-2 corresponding to the elaboration of the nanocrystals, a formation of new peaks appeared which have no relation with the previous ones and seem to be related to iron disulfide. It revealed the presence of triolite, marcasite phases and a pure pyrite at a high concentration of iron ions. The mixture of Fe-S compounds is probably due to the decomposition of pyrite and at a sulfidation temperature, the cubic phases are formed with no influence on the crystal structure since the calculated lattice constant a = 5.418 Å, is in good agreement with the pyrite phase cubic lattice parameter.

The scanning electron microscope observation showed a very promising nano structures, hexagonal morphology that changes into nanotubes by applying a magnetic field. While the XRD revealed different pyrite, triolite, and marcasite phases and their composition matching the data sheet references and previous studies.

Photoluminescence spectra allowed us to calculate the bad gap of samples Eg_1= 2.4 eV, Eg_2=2.3 eV with a slight difference caused by the variation of size grains. UV-Vis-IR demonstrated that pyrite in UV domain have maximum absorbance unlike IR.

Finally gas treatment helped us figure out that sample 2 reacts better with NO_x gas and sample 1 with CO_x.

References:

[1] G. Brostigen and a. Kjekshus, redetermined crystal structure of fes_2 (pyrite), acta chem. Scand. 23 (1969) no.6, https://doi.org/10.3891/acta.chem.scand.23-2186.

[2] Ms. Faber, m. A. Lukowski, q. Ding, n. S. Kaiser and s. Jin, earth-abundant metal pyrites (Fes_2 , Cos_2 , Nis_2 , and their alloys) for highly efficient hydrogen evolution and polysulfide reduction electrocatalysis, the journal of physical chemistry, august 29, 2014, http://dx.doi.org/10.1021/jp506288w.

[3] s. Zhao, s. Guo, c. Zhu, j. Gao, h. Li, h. Huang, y. Liu and z. Kang, achieving electroreduction of co2 to ch3oh with high selectivity using a pyrite–nickel sulfide nanocomposite, rsc adv., 2017, 7, 1376–1381, http://dx.doi.org/10.1039/c6ra26868d.

[4] Jian zou, jiacheng gao, preparation of nanosize iron pyrite fes2 and its properties, materials science forum vols. 610-613 (2009) pp 459-462, https://dx.doi.org/10.4028/www.scientific.net/msf.610-613.459.

[5] M. Zhang and h. Jiang, accurate prediction of band structure of fes2: a hard quest of advanced first-principles approaches, frontiers in chemistry 9 (2021) 747972 https://doi.org/10.3389/fchem.2021.747972

[6] S. Manzeli, d. Ovchinnikov, d. Pasquier, o.v. Yazyev and a. Kis, 2d transition metal dichalcogenides, nature reviews | materials 2017 volume 2 | article number 17033, https://doi.org/10.1038/natrevmats.2017.33.

[7] N. Berry, m. Cheng, c.l. Perkins, m. Limpinsel, j. C. Hemminger, and m. Law, atmospheric-pressure chemical vapor deposition of iron pyrite thin films, adv. Energy mater. 2012, https://doi.org/10.1002/aenm.201200043.

[8] X. Yao, f. Xia, a. P. Deditiusand j. Brugger, the mechanism and kinetics of the transformation from marcasite to pyrite: in situ and ex situ experiments and geological implications, contributions to mineralogy and petrology 2020,175(3), http://dx.doi.org/10.1007/s00410-020-1665-4.

[9] H. Qin, j. Jia, l. Lin, h. Ni, m. Wangb and l. Meng, pyrite fes2 nanostructures: synthesis, properties and applications, materials science and engineering: b volumes 236–237, october 2018, pages 104-124, https://doi.org/10.1016/j.mseb.2018.11.003

[10] H.r.barai, p. Barai, m.roy and s.w. Joo, nano-structural design of 0d, 1d, 2d, 3d nanoparticles for energy storage devices: supercapacitor applications, renewable energy and resources energy materials and fuel cell research 2nd international conference on & august 27-28, 2018, http://dx.doi.org/10.4172/2576-1463-c2-005.

[11] R.sai, h.ezzaouia and m.m.nofal, electronic structure of iron pyrite by the lmto_asa method, results in physics 22 (2021) 103950, https://doi.org/10.1016/j.rinp.2021.103950.

[12] G.l.zhao, j. Callaway, m. Hayashibara, electronic structures of iron and cobalt pyrites, physical review b, volume 48, issue 21, 1993, pages 15781-15786, https://doi.org/10.1103/physrevb.48.15781.

[13] W.m.temmerman, p.j.durham, d.j. Vaughan, the electronic structures of the pyrite-type disulphides (ms2, where m = mn, fe, co, ni, cu, zn) and the bulk properties of pyrite from local density approximation (lda) band structure calculations, physics and chemistry of minerals, volume 20, issue 4, september 1993, pages 248-254, https://doi.org/10.1007/bf00208138

[14] N. Ouarab, electronic and optical performance of ni-doped fes2 nanocrystals for photovoltaic applications, physica e: low-dimensional systems and nanostructures 115 (2020) 113688, https://doi.org/10.1016/j.physe.2019.113688.

[15] L. Yu , s. Lany , r. Kykyneshi , v. Jieratum , r. Ravichandran , b. Pelatt , e. Altschul , h. A. S. Platt , j. F. Wager , d. A. Keszler , a. Zunger , adv. Energy mater. 2011 , 1 , 748, https://doi.org/10.1002/aenm.201100351.

[16] R.sun , m. K. Y. Chan , g. Ceder , phys. Rev. B 2011 , 83 , 235311, https://doi.org/10.1103/physrevb.83.235311.

[17] p.k. Abraitis, r.a.d. Pattrick, d.j. Vaughan, variations in the compositional, textural and electrical properties of natural pyrite: a review, international journal of mineral processing volume 74, issues 1–4, 19 november 2004, pages 41-59, https://doi.org/10.1016/j.minpro.2003.09.002.

[18] D. F. Pridmore; r. T. Shuey, the electrical resistivity of galena, pyrite, and chalcopyrite, american mineralogist (1976) 61 (3-4): 248–259. Https://doi.org/10.1016/j.minpro.2003.09.002.

[19] Schieck, r., hartmann, a., fiechter, s., konenkamp, r., wetzel, h., 1990. Electrical properties of natural and synthetic pyrite (fes2) crystals. Journal materials research 5, 1567 – 1572. Https://doi.org/10.1557/jmr.1990.1567

[20] Doyle, f.m., mirza, a.h., 1996. Electrochemical oxidation of pyrite samples with known composition and electrical properties. Electrochemical proceedings 96 (6), 203 – 214, https://doi.org/10.1016/j.minpro.2003.09.002.

[21] P.a. Kyriacou and s. Chatterjee, the origin of photoplethysmography, photoplethysmography technology, signal analysis and applications 2022, pages 17-43, https://doi.org/10.1016/b978-0-12-823374-0.00004-9.

[22] P.p.altermatt, t.kiesewetter, k.ellmer and h.tributsch, specifying targets of future research in photovoltaic devices containing pyrite (fes2) by numerical modelling, solar energy materials and solar cells volume 71, issue 2, 1 february 2002, pages 181-195, https://doi.org/10.1016/s0927-0248(01)00053-8.

[23] Q.yu, s. Cai, z. Jin, z. Yan, evolutions of composition, microstructure and optical properties of mn-doped pyrite (fes2) films prepared by chemical bath deposition, materials research bulletin volume 48, issue 9, september 2013, pages 3601-3606, https://doi.org/10.1016/j.materresbull.2013.05.074.

[24] R. Khandaker, m. Kamruzzaman, m. Afrose, r. Rahman, m. Khan, m.k.r. Khan, m. N. H. Liton, m.a. Helal, t. K. Anam and m. M. Rahman, enhanced optical properties of fes2 using ni@cu doping and characterization of the structural and chemical compositions for solar cell applications, crystallography reports vol. 65 (2020), no. 6, pp. 968–979, https://doi.org/10.1134/s1063774520060188.

[25] S. Miyahara and t. Teranishi, magnetic properties of FeS_2 and Cos_2, journal of applied physics 1 february 1968 volume 39, number 2, https://doi.org/10.1063/1.1656326.

[26] k.e.waters, n.a.rowson, r.w.greenwood, a.j.williams, the effect of heat treatment on the magnetic properties of pyrite, minerals engineering volume 21, issue 9, august 2008, pages 679-682, https://doi.org/10.1016/j.mineng.2008.01.008.

[27] H.moselmi and m.gharabaghi, a review on electrochemical behavior of pyrite in the froth flotation process,journal of industrial and engineering chemistry volume 47, 25 march 2017, pages 1-18, https://doi.org/10.1016/j.jiec.2016.12.012.

[28] X. Chen, z. Wang, x. Wang, j. Wan, j. Liu, and y. Qian, single-source approach to cubic fes2 crystallites and their optical and electrochemical properties, inorg. Chem, 44, (2005), 951−954, https://doi.org/10.1021/ic049049m.

[29] h.b. Bebb, e.w.williams, chapter 4 photoluminescence i: theory, semiconductors and semimetals volume 8, 1972, pages 181-320, https://doi.org/10.1016/s0080-8784(08)62345-5.

[30] m.a. Khan, j.c.sarker, s. Lee, s.c.mangham, m.o. Manasreh, synthesis, characterization and processing of cubic iron pyrite nanocrystals in a photovoltaic cell, materials chemistry and physics volume 148, issue 3, 15 december 2014, pages 1022-1028, https://doi.org/10.1016/j.matchemphys.2014.09.013.

[31] Md. Wasi ahmad, umme farva and m. Alam khan, low temperature synthesis of iron pyrite (fes2) nanospheres as a strong solar absorber material, materials letters (2018), https://doi.org/10.1016/j.matlet.2018.06.001.

[32] A.j.j. Bos, theory of thermoluminescence, radiation measurements 41 (2007) s45 – s56, https://doi.org/10.1016/j.radmeas.2007.01.003.

[33] A.n. Silverman, p.w. Levy and j.a.kierstead, thermoluminescence kinetics of pyrite (fes2), international journal of radiation applications and instrumentation. Part d. Nuclear tracks and radiation measurements volume 18, issues 1–2, 1991, pages 53-60, https://doi.org/10.1016/1359-0189(91)90092-v.

[34] Z.Zhou and C.Uher, apparatus for seebeck coefficient and electrical resistivity measurements of bulk thermoelectric materials at high temperature, review of scientific instruments 76, 023901 (2005), https://doi.org/10.1063/1.1835631.

[35] H. Julian goldsmid, introduction to thermoelectricity, springer-verlag berlin heidelberg (2016), https://doi.org/10.1007/978-3-662-49256-7

[36] I. Harran, y. Li, h. Wang, y. Chen and y. Ni, iron disulfide compound: a promising thermoelectric material, materials research express, volume 4 (2017), number 10 , https://doi.org/10.1088/2053-1591/aa90a1.

[37] S. Liu, y. Li, j. Yang, h. Tian, b. Zhu, y. Shi, first- principles study of high-pressure stability, structure, and elasticity of fes2 polymorphs, phys chem minerals (2014) 41:189–196, https://doi.org/10.1007/s00269-013-0637-x.

[38] E.j.hearnph.d, b.sc. (eng.) Hons, c.eng, f.i.mech.e, f.i.prod.e and f.i.diag.e,, chapter 1-simple stress and strain, mechanics of materials 1 (third edition) an introduction to the mechanics of elastic and plastic deformation of solids and structural materials 1997, pages 1-26, https://doi.org/10.1016/b978-075063265-2/50002-5.

[39] O.o. Abegunde, e.t. Akinlabi, o.p. Oladijo, s. Akinlabi and a.u. Ude, overview of thin film deposition techniques, aims materials science (13 march 2019), 6(2): 174–199. Https://doi.org/10.3934/matersci.2019.2.174.

[40] K.o. Ukoba , a.c. Eloka-eboka and f.l. Inambao, review of nanostructured nio thin film deposition using the spray pyrolysis technique, , renewable and sustainable energy reviews (2017), http://dx.doi.org/10.1016/j.rser.2017.10.041.

[41] A.v. Rane, k.kanny, v.k. Abitha and s. Thomas, chapter 5 methods for synthesis of nanoparticles and fabrication of nanocomposites, https://doi.org/10.1016/b978-0-08-101975-7.00005-1.

[42] A.p. Periyasamy, m. Venkataraman, d. Kremenakova, j. Militky and y. Zhou, progress in sol-gel technology for the coatings of fabrics, materials 2020, 13(8), 1838; https://doi.org/10.3390/ma13081838.

[43] T.dhandayuthapani, m.girish, r.sivakumar, c.sanjeeviraja and r.gopalakrishnan, tuning the morphology of metastable mns films by simple chemical bath deposition technique, applied surface science volume 353, 30 october 2015, pages 449-458, https://doi.org/10.1016/j.apsusc.2015.06.154.

[44] J b mooney, s b radding, spray pyrolysis processing, annual review of materials science 1982 vol. 12:81-101, https://doi.org/10.1146/annurev.ms.12.080182.000501.

[45] R.smith, h.iinomata and c.peters, chapter 4 - historical background and applications, supercritical fluid science and technology volume 4, 2013, pages 175-273, https://doi.org/10.1016/b978-0-444-52215-3.00004-0

[46] L.a.neacşu, a.i.nicoară, o.r.vasile, b.ş.vasile, chapter 9 - inorganic micro- and nanostructured implants for tissue engineering, nanobiomaterials in hard tissue engineering applications of nanobiomaterials volume 4 2016, pages 271-295, https://doi.org/10.1016/b978-0-323-42862-0.00009-2.

[47] A.sarangan, 5 - nanofabrication, fundamentals and applications of nanophotonics 2016, pages 149-184, https://doi.org/10.1016/b978-1-78242-464-2.00005-1.

[48] G.faraji, h.s.kim, h.t.kashi, introduction, severe plastic deformation methods, processing and properties 2018, pages 1-17, https://doi.org/10.1016/b978-0-12-813518-1.00020-5.

[49] A.bashir, t.i.awan, a.tehseen, m.b.tahir, m.ijaz, chapter 3 - interfaces and surfaces, chemistry of nanomaterials fundamentals and applications 2020, pages 51-87, https://doi.org/10.1016/b978-0-12-818908-5.00003-2.

[50] S.ebnesajjad, 4 - surface and material characterization techniques, handbook of adhesives and surface preparation technology, applications and manufacturing plastics design library 2011, pages 31-48, https://doi.org/10.1016/b978-1-4377-4461-3.10004-5.

[51] P.s.goh, a.f.ismail, b.c.ng, chapter 2 - raman spectroscopy, membrane characterization 2017, pages 31-46, https://doi.org/10.1016/b978-0-444-63776-5.00002-4

[52] E.stauffer, j.a.dolan, r.newman, chapter 8 - gas chromatography and gas chromatography—mass spectrometry, fire debris analysis 2008, pages 235-293, https://doi.org/10.1016/b978-012663971-1.50012-9

[53] A.a. Bunaciu,e.g. Udriştioiu and h.y. Aboul-enein, x-ray diffraction: instrumentation and applications, critical reviews in analytical chemistry, 2015 45:4, 289-299, https://doi.org/10.1080/10408347.2014.949616.

[54] P.scardi and m. Leoni, diffraction line profiles from polydisperse crystalline systems, october 2001acta crystallographica. Section a, foundations of crystallography 57(5):604-613, https://doi.org/10.1107/s0108767301008881.

[55] S. Ray, 4 - techniques for characterizing the structure and properties of polymer nanocomposites, environmentally friendly polymer nanocomposites types, processing and properties woodhead publishing series in composites science and engineering 2013, pages 74-88, https://doi.org/10.1533/9780857097828.1.74.

[56] M.a.mohamed, j.jaafar, a.f.ismail, m.h.d.othman, m.a.rahman, chapter 1 - fourier transform infrared (ftir) spectroscopy, membrane characterization 2017, pages 3-29, https://doi.org/10.1016/b978-0-444-63776-5.00001-2.

[57] A.b.d. Nandiyanto, r.okitiani and r.ragadhita, how to read and interpret ftir spectroscope of organic materia, urnal of science & technology,volume 4 issue 1, april 2019 pag, http://dx.doi.org/10.17509/ijost.v4i1.xxxx.

[58] M. Picollo, m.aceto and t. Vitorino, uv-vis spectroscopy, physical sciences reviews. 2018; 20180008, https://doi.org/10.1515/psr-2018-0008.

[59] K.dyamenahalli, a.famili, r.shandas, 3 - characterization of shape-memory polymers for biomedical applications, shape memory polymers for biomedical applications woodhead publishing series in biomaterials 2015, pages 35-63, https://doi.org/10.1016/b978-0-85709-698-2.00003-9.

[60] D.r.baer, s.thevuthasan, chapter 16 - characterization of thin films and coatings, handbook of deposition technologies for films and coatings (third edition) science, applications and technology 2010, pages 749-864, https://doi.org/10.1016/b978-0-8155-2031-3.00016-8.

[61] S.eaton-magaña and c.m. Breeding, an introduction to photoluminescence spectroscopy for diamond and its applications in gemology, gems & gemology 2016, vol. 52, no. 1, pp. 2–17, http://dx.doi.org/10.5741/gems.52.1.2.

[62] Adrie j. J. Bos, thermoluminescence as a research tool to investigate luminescence mechanisms, materials 2017, 10, 1357, https://doi.org/10.3390/ma10121357.

[63] P. S.kumar, k.g.pavithra, mu.naushad, chapter 4 - characterization techniques for nanomaterials, nanomaterials for solar cell applications 2019, pages 97-124, https://doi.org/10.1016/b978-0-12-813337-8.00004-7.

[64] J. A. Nieto, thermoluminescence dosimetry (tld) and its application in medical physics, aip conference proceedings (2004) 724, 20; https://doi.org/10.1063/1.1811814.

[65] N.s.rawat, m.s.kulkarni,d.r.mishra and b.c.bhatt, an attempt to correlate shift in thermoluminescence peak with heating rate and black body radiation, april 2014, https://doi.org/10.4103/0972-0464.147273.

[66] G. F. J. Garlick and maurice hugh frederick wilkins, short period phosphorescence and electron traps, november 1945 https://doi.org/10.1098/rspa.1945.0026.

[67] R. P. Johnson, "luminescence of sulphide and silicate phosphorse", j. Opt. Soc. Am., 29 (1939) 387, https://doi.org/10.1364/josa.29.000387.

[68] Andrew h.simon, chapter 7 - sputter processing, handbook of thin film deposition (fourth edition) 2018, pages 195-230, https://doi.org/10.1016/b978-0-12-812311-9.00007-4.

[69] M.uo, t.wada, t.sugiyama,applications of x-ray fluorescence analysis (xrf) to dental and medical specimens, japanese dental science review volume 51, issue 1, february 2015, pages 2-9, https://doi.org/10.1016/j.jdsr.2014.07.001

[70] A.behnamfrad, k.chegni, r.alaei and f.veglio, the efect of thermal and acid treatment of kaolin on its ability for cyanide removal from aqueous solutions, environmental earth sciences (2019) 78:408, https://doi.org/10.1007/s12665-019-8408-8.

[71] E.klosek-wawrzyn, j.malolepszy and p.murzyn, sintering behavior of kaolin with calcite, procedia engineering 57 (2013) 572 – 582, https://doi.org/10.1016/j.proeng.2013.04.073

[72] A. Vedavathia ,y.m. Reddy and k.t.reddy, effect of precursor concentration on structural and morphological properties of iron pyrite thin films, procedia materials science 10 (2015) 279 – 284, https://doi.org/10.1016/j.mspro.2015.06.051.

[73] S.wang and j.yu, electrochemical mechanism for fes2/c composite in lithium ion batteries with enhanced reversible capacity, energies 2016, 9, 225; https://doi.org/10.3390/en9040225.

[74] P. Prabukanthan, r. J. Soukup, n. J. Lanno, a. Sarffr, s. Kment, h. Kmentova, c. A. Kamler, c. L. Exstrom, j. Olejnicek and s. A. Oarveau, chemical bath deposition (cbd) of iron sulfide thin films for photovol talc applications, crystallographic and optical properties, https://doi.org/10.1109/PVSC.2010.5614465.

[75] M.wang, d.xue, h.qin, l.zhang, g.ling, j.liu, y.fang and l.meng, preparation of fes2 nanotube arrays based on layer-by-layer assembly and their photoelectrochemical

properties,materials science and engineering b 204 (2016) 38-44, https://doi.org/10.1016/j.mseb.2015.11.008.

[76] F.huang, w.gao, s.gao, l.meng, z.zhang, y.yan, y.ren, y.li, k.liu, m.xing and y.wang, morphology evolution of nano-micron pyrite: a review, journal of nanoscience and nanotechnology vol. 17, 5980–5995, 2017 https://doi.org/10.1166/jnn.2017.14430.

[77] E.m.marti, s.g.martinez, c.g.lozano and m.p.zorzano, pyrite-induced uv-photocatalytic abiotic nitrogen fixation: implications for early atmospheres and life, scientific reports (2019) 9:15311, https://doi.org/10.1038/s41598-019-51784-8.

[78] J.rashid, s.saleem, s.u.awan, a.iqbal, r.kumar, m.a.barakat, m.arshad, m.zaheer, m.rafique and m.awad, stabilized fabrication of anatase-tio2/fes2 (pyrite) semiconductor composite nanocrystals for enhanced solar light-mediated photocatalytic degradation of methylene blue, rsc adv., 2018, 8, 11935, https://doi.org/10.1039/c8ra02077a.

[79] F.jiang, l.t.peckler and a.j.muscat, phase pure pyrite fes2 nanocubes synthesized using oleylamine as ligand, solvent,and reductant, cryst. Growth des 23 jun 2015 1-29, https://doi.org/10.1021/acs.cgd.5b00751.

[80] C.wang, l.yin, l.zhang, d.xiang and r.gao, metal oxide gas sensors: sensitivity and influencing factors, sensors 2010, 10, 2088-2106; https://doi.org/10.3390/s100302088.

[81] Feroz A. Mir, Transparent wide band gap crystals follow indirect allowed transition and bipolaron hopping mechanism, F.A. Mir / Results in Physics 4 (2014) 103–104, http://dx.doi.org/10.1016/j.rinp.2014.06.001